

Research Articles | Systems/Circuits

Oscillatory waveform shape and temporal spike correlations differ across bat frontal and auditory cortex

<https://doi.org/10.1523/JNEUROSCI.1236-23.2023>

Received: 3 July 2023

Revised: 1 November 2023

Accepted: 29 November 2023

Copyright © 2024 the authors

This Early Release article has been peer reviewed and accepted, but has not been through the composition and copyediting processes. The final version may differ slightly in style or formatting and will contain links to any extended data.

Alerts: Sign up at www.jneurosci.org/alerts to receive customized email alerts when the fully formatted version of this article is published.

1 Oscillatory waveform shape and temporal spike correlations differ across
2 bat frontal and auditory cortex

3
4 **Abbreviated title:** Oscillatory waveform shape in the bat cortex

5 **Authors:** Francisco García-Rosales^{1§}, Natalie Schaworonkow^{1*}, Julio C. Hechavarria^{2*§}.

6 **Affiliations:** ¹ Ernst Strüngmann Institute (ESI) for Neuroscience in Cooperation with Max Planck Society, 60528 Frankfurt am Main,
7 Germany; ² Institut für Zellbiologie und Neurowissenschaft, Goethe-Universität, 60438 Frankfurt/M., Germany.

8 * *Authors contributed equally to this work.*

9 § *Corresponding authors.*

10
11 **Mailing address:** Francisco García-Rosales, Ernst Strüngmann Institute (ESI) for Neuroscience in Cooperation with Max Planck
12 Society, Deutschordenstraße 46, 60528 Frankfurt am Main, Germany; Tel. (+49) 69 / 96769 123. Email: [francisco.garcia-](mailto:francisco.garcia-rosales@esi-frankfurt.de)
13 rosales@esi-frankfurt.de

14
15
16 **Number of pages:** 35

17 **Number of figures:** 9

18 **Number of words (Abstract):** 211

19 **Number of words (Introduction):** 650

20 **Number of words (Discussion):** 1425

21 **Conflict of interests:** The authors declare no conflicting financial or non-financial interests.

22 **Acknowledgments:** This work was supported by the DFG (Grant No. HE 7478/1-1, to J.C.H.), the Joachim-Herz Foundation
23 (fellowship granted to F.G.R.), and a Marie Skłodowska-Curie Actions Postdoctoral Fellowship (grant No. 101062497, to N.S.).

26 **Abstract**

27 Neural oscillations are associated with diverse computations in the mammalian brain. The waveform
28 shape of oscillatory activity measured in cortex relates to local physiology, and can be informative about
29 aberrant or dynamically changing states. However, how waveform shape differs across distant yet
30 functionally and anatomically related cortical regions is largely unknown. In this study, we capitalize on
31 simultaneous recordings of local field potentials (LFPs) in the auditory and frontal cortices of awake, male
32 *Carollia perspicillata* bats to examine, on a cycle-by-cycle basis, waveform shape differences across
33 cortical regions. We find that waveform shape differs markedly in the fronto-auditory circuit even for
34 temporally correlated rhythmic activity in comparable frequency ranges (i.e. in the delta and gamma
35 bands) during spontaneous activity. In addition, we report consistent differences between areas in the
36 variability of waveform shape across individual cycles. A conceptual model predicts higher spike-spike
37 and spike-LFP correlations in regions with more asymmetric shape, a phenomenon that was observed in
38 the data: spike-spike and spike-LFP correlations were higher in frontal cortex. The model suggests a
39 relationship between waveform shape differences and differences in spike correlations across cortical
40 areas. Altogether, these results indicate that oscillatory activity in frontal and auditory cortex possess
41 distinct dynamics related to the anatomical and functional diversity of the fronto-auditory circuit.

42

43 **Significance statement**

44 The brain activity of many animals displays intricate oscillations, which are usually characterized in terms
45 of their frequency and amplitude. Here, we study oscillations from the bat frontal and auditory cortices on
46 a cycle-by-cycle basis, additionally focusing on their characteristic waveform shape. The study reveals
47 clear differences across regions in waveform shape and oscillatory regularity, even when the frequency of
48 the oscillations is similar. A conceptual model predicts that more asymmetric waveforms result from
49 stronger correlations between neural spikes and electrical field activity. Such predictions were supported
50 by the data. The findings shed light onto the unique properties of different cortical areas, providing key
51 insights into the distinctive physiology and functional diversity within the fronto-auditory circuit.

52 Introduction

53 Rhythmic neural activity at various timescales underpins several functions in the mammalian brain. In the
54 frontal cortex, oscillations of local-field potentials (LFPs) in low and high frequencies are implicated in
55 cognitive and executive control (Helfrich and Knight, 2019; Insel et al., 2012; Rajan et al., 2019; Tavares
56 and Tort, 2022; Veniero et al., 2021; Zhang et al., 2016), while rhythmic activity in sensory cortices is
57 linked with the effective encoding of incoming stimuli (Gourevitch et al., 2020; Gross et al., 2007; Kienitz
58 et al., 2021; Lakatos et al., 2007; Tan et al., 2019; Teng et al., 2017; Uran et al., 2022). These oscillations
59 reflect the underlying dynamics of their generating motifs, which determine several of their properties,
60 including waveform shape (Cole and Voytek, 2017). Indeed, waveform shape and related features
61 change in the developing brain (Schaworonkow and Voytek, 2021) and possess atypical characteristics in
62 disease (Cole and Voytek, 2019; Cole et al., 2017; Jackson et al., 2019). Waveform patterns of oscillatory
63 activity can provide important insights into the physiology and function of the neocortex, yet how they
64 differ across cortical regions remains largely unstudied.

65 In this work, we examine oscillatory waveform shape in the frontal and auditory cortices of a mammalian
66 vocal specialist, the bat *Carollia perspicillata*. The bat auditory cortex (AC) is a well-studied structure that
67 presents both spontaneous and stimulus-driven rhythmic patterns of neuronal activity (Garcia-Rosales et
68 al., 2019; Hechavarria et al., 2016; Medvedev and Kanwal, 2004). As in other mammals (Lakatos et al.,
69 2005; Luo and Poeppel, 2007; Neymotin et al., 2022; Teng et al., 2017), LFPs in the bat AC track the
70 temporal dynamics of acoustic sequences with periodic and quasi-periodic temporal structures (Garcia-
71 Rosales et al., 2018). LFPs in *C. perspicillata*'s AC exhibit clear coupling with neuronal spiking, potentially
72 coordinating single-cell responses to acoustic stimuli and contributing actively to the encoding of multi-
73 syllabic communication sounds (Garcia-Rosales et al., 2018).

74 In the frontal cortex, we focused on the frontal auditory field (FAF), a structure specialized in auditory-
75 related behaviour (Eiermann and Esser, 2000; Kanwal et al., 2000; Kobler et al., 1987). This region is
76 anatomically connected with the AC, but receives also relatively fast inputs from an alternative pathway
77 bypassing midbrain and cortex (Kobler et al., 1987). Pre- and post-vocal dynamics in the FAF, as well as
78 its functional connectivity patterns with the AC and the striatum, implicate this region in the control of
79 vocalization behaviour (Garcia-Rosales et al., 2022b; Weineck et al., 2020). Furthermore, the FAF is
80 anatomically connected with the superior colliculus, suggesting that it may be involved in coordinating fast
81 movements based on the bat's auditory environment (Casseday et al., 1989; Kobler et al., 1987). The
82 nature of FAF-AC interconnectivity suggests that the FAF plays a crucial role in the integration of auditory
83 feedback for the coordination of rapid auditory-based behaviour (Garcia-Rosales et al., 2022b). These
84 data indicate that, while the AC operates as a classical sensory cortex, the FAF acts as part of a control
85 and integration hub.

86 While low- and high-frequency oscillatory activities in the bat FAF-AC network are functionally related, it is
87 unknown how they differ in terms of waveform shape. Characterizing waveform shape differences across
88 cortical regions could be an informative step towards understanding how neuronal oscillations in these
89 areas differ, and thus constrain hypotheses about the mechanisms underlying neural activity across
90 structures. By means of simultaneous electrophysiological recordings and cycle-by-cycle analyses of
91 neural oscillations, we show that the waveform shape and variability of frontal- and auditory-cortical
92 oscillations differ markedly in delta and gamma frequencies. We demonstrate a relationship between
93 waveform shape and spike correlations by modelling and computing spike-field measures. We argue that
94 these differences reflect physiological disparities in the FAF-AC circuit, and establish a potential link
95 between spike timing and waveform shape. Our results support the notion of heterogeneity of cortical
96 rhythms in the mammalian brain, and stress the importance of waveform shape for understanding cortical
97 physiology and function.

98 **Materials and Methods**

99 Animal preparation and surgical procedures

100 The study was conducted on two awake *Carollia perspicillata* bats (2 males), which were obtained from a
101 colony at the Goethe University, Frankfurt. All experimental procedures were in compliance with
102 European regulation and were approved by the relevant local authorities (Regierungspräsidium
103 Darmstadt, experimental permit #FU-1126). Animals used in experiments were kept isolated from the
104 main colony, with a reversed light-dark cycle (i.e. lights off from 12:00 to 00:00; this applies to all bats in
105 the colony as well).

106 The data presented in this work were collected as part of a previous study (Garcia-Rosales et al., 2022b),
107 where a detailed description of the surgical procedures can be found. In brief, bats were anesthetized
108 with a mixture of ketamine ($10 \text{ mg} \cdot \text{kg}^{-1}$, Ketavet, Pfizer) and xylazine ($38 \text{ mg} \cdot \text{kg}^{-1}$, Rompun, Bayer), and
109 underwent surgery in order to expose the skull in the areas of the frontal and auditory cortices. A metal
110 rod (ca. 1 cm length, 0.1 cm diameter) was glued onto the bone for head fixation during
111 electrophysiological recordings. A local anaesthetic (ropivacaine hydrochloride, 2 mg/ml, Fresenius Kabi,
112 Germany) was applied subcutaneously around the scalp area prior any handling of the wounds. The
113 precise locations of the FAF and AC were determined by means of well-described landmarks, including
114 the sulcus anterior and prominent blood vessel patterns (Eiermann and Esser, 2000; Esser and
115 Eiermann, 1999; Garcia-Rosales et al., 2020). Access to the frontal and auditory regions of the left
116 hemisphere was gained by cutting small holes (ca. 1 mm^2) with a scalpel blade on the first day of
117 recordings. Electrophysiological recordings in the AC were made mostly in the high frequency fields
118 (Esser and Eiermann, 1999).

119 After the surgery animals were given sufficient time to recover (no less than 2 days) before the beginning
120 of experimental sessions. A session did not last more than 4 hours per day. Water was offered to the bats
121 every 1 – 1.5 hours. Experiments were halted if an animal showed any signs of discomfort (e.g. as
122 excessive movement). No animal was used on two consecutive days for recordings.

123 Electrophysiological recordings

124 Electrophysiological measurements were made acutely from fully awake animals in a sound-proofed and
125 electrically isolated chamber. Inside the chamber, bats were placed on a custom-made holder kept at a
126 constant temperature of 30 °C using a heating blanket (Harvard, Homeothermic blanket control unit).
127 Data were acquired simultaneously from the FAF and AC of the left hemisphere using two 16-channel
128 laminar probes (Model A1x16, NeuroNexus, MI; 50 µm channel spacing, impedance: 0.5–3 MΩ per
129 electrode). For each paired FAF-AC recording, probes were carefully inserted into the tissue using piezo
130 manipulators (one per probe; PM-101, Science products GmbH, Hofheim, Germany), perpendicular to the
131 cortical surface, until the top channel was barely visible above the surface. The typical width of *C.*
132 *perspicillata*'s cortex, and the total span of the electrodes in the probes (750 µm) allowed us to record
133 from all six cortical layers at once (see Garcia-Rosales et al. (2022b); Garcia-Rosales et al. (2019)). From
134 one paired recording to the next in the same experimental session, probes were retracted from the
135 cortical tissue and moved to a new location within the craniotomy in FAF or AC, as distant as possible
136 from previous recording sites within that craniotomy. New recording locations were chosen at the
137 beginning of each experimental session.

138 Probes in FAF and AC were connected to micro-preamplifiers (MPA 16, Multichannel Systems MCS
139 GmbH, Reutlingen, Germany), while acquisition was done with a single 32-channel system with
140 integrated digitization (sampling frequency, 20 kHz; precision, 16 bits) and amplification steps (Multi
141 Channel Systems MCS GmbH, model ME32 System, Germany). Silver wires were used as references
142 electrodes for each recording shank (i.e. in FAF and AC) placed at different areas of the brain (for FAF:
143 non-auditory lateral ipsilateral region; for AC: non-auditory occipital ipsilateral region). The silver wires
144 were carefully positioned between the skull and the dura matter. The reference and the ground of each
145 probe were short-circuited, and the ground was ultimately common in the acquisition system (the ME32).
146 Recordings were monitored online and stored in a computer using the MC_Rack_Software (Multi Channel
147 Systems MCS GmbH, Reutlingen, Germany; version 4.6.2). Due to technical reasons, the signal from one
148 FAF channel (depth: 500 µm) was linearly interpolated from its immediate neighbours.

149 Pre-processing of spiking and LFP signals

150 All data analyses were made using custom-written Python scripts. Raw data from the recording system
151 were converted to H5 format using Multichannel System's *McsPyDataTools* package
152 (<https://github.com/multichannelsystems/McsPyDataTools>, version 0.4.3), and were then parsed and

153 handled with *Syncopy* (<https://github.com/esi-neuroscience/syncopy>, version 2022.8). Local-field
154 potentials were obtained by filtering the raw data with a low pass Butterworth filter (4th order) with a cut-off
155 frequency of 300 Hz. For computational convenience, LFP signals were then downsampled to 5 kHz. On
156 occasions a sharp spectral peak at 100 Hz was present in the recordings, corresponding to a harmonic of
157 the line noise. We were discouraged to use LFPs close (or above) to 100 Hz in the analyses for the
158 following reasons: (i) frequencies close to 100 Hz would be affected by the line noise harmonic; and (ii)
159 high frequency LFPs (> 100 Hz) can be directly influenced by spiking activity in the form of, for example,
160 spike-bleed through (Ray, 2015). Spike bleed-through constitutes a potential confound that we sought to
161 avoid.

162 For the detection of multi-unit activity, the raw data was bandpass filtered between 300 and 3000 Hz with
163 a 4th order Butterworth filter. Spikes were detected based on threshold crossing: we defined a spike as a
164 peak with an amplitude of at least 3.5 standard deviations relative all samples in the signal. Only peaks
165 separated by at least 2 ms were considered.

166 Spectral analyses

167 Power spectral densities (PSDs) were computed using Welch's method (segment length 20480 samples,
168 i.e. 4096 ms) implemented in *scipy* (version 1.9.1). PSDs were calculated independently for each LFP
169 trace (all channels in the N = 29 recordings in both FAF and AC). LFP traces were typically *circa*, but not
170 shorter than, 1200 s long (median: 1239.5 s; 25th percentile: 1252.8 s; 75th percentile: 1423.9 s). The
171 power of each recording was parametrized using a spectral parametrization model (Donoghue et al.,
172 2020), with which a 1/f fit of the PSD was computed. All fits had an $R^2 > 0.93$ (mean: 0.9965, s.e.m.:
173 0.001).

174 We reasoned that significant deviations of the power spectrum from the 1/f fit potentially represented
175 oscillatory activity at a given frequency range. Thus, we normalized each power spectrum by its 1/f
176 component to highlight spectral peaks in FAF and AC. Normalized values would hover around 0 in the
177 case of no spectral peaks, and would be consistently greater than 0 for frequencies in which LFPs
178 presented clear deviations from the underlying 1/f trend. For each channel, we considered a significant
179 deviation from the 1/f if the normalized power at a certain frequency was significantly larger than 0 (FDR-
180 corrected, two-sided one-sample t-tests, $p_{\text{corr}} < 0.05$). This analysis was done for each individual animal
181 (Bat-01, N = 15; Bat-02, N = 14), for frequencies ranging from 1 to 120 Hz. From the results in the two
182 bats, we established the following frequency bands of interest: delta (1–4 Hz) and gamma (65–85 Hz).

183 Cycle-by-cycle analyses

184 For detecting oscillatory bursts in the frequencies of interest we used the *bycycle* package ((Cole and
185 Voytek, 2019), version 1.0.0). The *bycycle* algorithm makes it possible to detect individual cycles in
186 frequency range of interest (here, the frequency bands outlined above), and then to determine whether

187 detected cycles belong to so-called “oscillatory bursts”. An oscillatory burst consists of a sequence of
188 cycles (at least 3 in this study) with stable temporal properties that are mainly summarized as follows:
189 amplitude consistency, period consistency, and monotonicity (rise and decay flanks of cycles in a burst
190 should be mostly monotonic). Furthermore, one parameter controls for signal-to-noise ratio (SNR): the
191 amplitude fraction threshold (see **Fig. 2A**). This parameter rejects cycles whose amplitudes are below a
192 certain percentile relative to the amplitude of all cycles in a given trace. As in (Schaworonkow and Voytek,
193 2021), we chose the following thresholds for cycle detection: Amplitude fraction threshold, 0.5; Amplitude
194 consistency threshold, 0.5; Period consistency threshold, 0.5; Monotonicity threshold, 0.5.

195 Each cycle was characterized according to the following features, which determine waveform shape:
196 cycle period (i.e. the duration of each cycle), cycle rise-decay asymmetry (the asymmetry between rise
197 and decay times in the cycle), and cycle peak-trough asymmetry (the asymmetry in duty cycle; see also
198 (Cole and Voytek, 2019; Schaworonkow and Voytek, 2021)). Bursts were characterized according to their
199 duration (the sum of the individual duration of each cycle in the burst). Only cycles that were part of
200 oscillatory bursts were used for further analyses.

201 To compare cycle features across different recording sites (e.g. between channels in FAF and AC), we
202 defined the value of a given feature for a certain recording as the median value of that feature across all
203 detected cycles in the recording. This was made per LFP trace, therefore yielding one value per recording
204 site (N = 29 paired FAF-AC sites, across 16 channels; data from the two bats were pooled as spectral
205 and bursting patterns were highly consistent across animals). Given that data from FAF and AC were
206 acquired simultaneously for each paired recording, the above allowed us to compare across sites using
207 paired statistics (FDR-corrected Wilcoxon signed-rank tests, significant for $p_{\text{corr}} < 0.05$). Only values
208 derived from simultaneously recorded LFP traces were compared to one another.

209 A median asymmetry value of 0.5 for a given LFP trace indicates that cycles tend towards a sinusoidal
210 shape. The farther the value is from 0.5 (above or below) the more asymmetric a waveform is. However,
211 whether such values lie above or below the 0.5 threshold strongly depends on signal polarity. Note, for
212 example, that a certain signal and its copy, the latter with inverse polarity, will have values of asymmetry
213 equally distanced from 0.5, but in opposite directions (as peaks become troughs with a polarity inversion).
214 Thus, not controlling for signal polarity can be a strong confound when comparing waveform shape
215 asymmetries, especially if these are calculated from electrodes located in different brain regions which
216 already have dissimilar cytoarchitectures, such as the frontal and auditory cortices. Since we are unable
217 to control for signal polarity in the current dataset, we avoid this potential confound by normalizing median
218 asymmetry values to 0.5. That is, the asymmetry value for a given LFP trace used for comparisons is
219 given by the absolute value of the difference between its raw asymmetry and 0.5. This approach
220 measures how far from sinusoidal the waveform shape of an LFP trace is, independently of signal polarity

221 (Schaworonkow and Voytek, 2021), and is therefore better suited for inter-areal comparisons of waveform
222 shape asymmetry.

223 The aforementioned cycle features characterize waveform shape, but they do not quantify to what degree
224 individual burst cycles in a given LFP trace are similar to one another. This is measured by the dispersion
225 of the distribution of the cycle features, which was quantified here as the coefficient of variation (CV). The
226 CV is computed over each LFP trace, therefore quantifying cycle-by-cycle the variability over time; it is
227 expressed as follows:

$$228 \quad CV = \frac{\sigma_W}{\mu_W}, \quad [1]$$

229 where σ_W is the standard deviation of the cycle feature distribution (W), and μ_W its mean.

230 Every recording in frontal or auditory cortex had a specific CV for a given cycle parameter, channel and
231 frequency band. As described with median feature values, this enabled us to conduct paired statistics
232 when comparing CV values between FAF and AC (FDR-corrected Wilcoxon signed-rank tests, significant
233 for $p_{\text{corr}} < 0.05$). The CV was calculated from raw feature values (not normalized to 0.5) across all cycles
234 in a given signal, given that this metric is not affected by signal polarity as it is self-contained for each LFP
235 trace. This allows to explore cycle-by-cycle variability over time without affecting the individual asymmetry
236 values of the cycles involved.

237 Sensitivity analyses

238 To evaluate the dependence of significant differences across cortical structures on the burst detection
239 parameters of the *bycycle* algorithm, bursts were detected as above but detection parameters were
240 varied in pairs as follows: (i) amplitude fraction threshold vs. amplitude consistency threshold; (ii)
241 amplitude fraction threshold vs. period consistency threshold; and (iii) amplitude fraction threshold vs.
242 monotonicity threshold. The same parameter values were used to detect bursts in FAF and AC. However,
243 we also evaluated to what degree our results were sensitive to different burst detection parameters
244 across regions, varying the amplitude fraction threshold independently in each area (**Fig. 7**). Parameters
245 were varied in the range from 0.1 to 0.9, with a step of 0.1. All waveform features were computed as
246 described above, and the variability of waveform features was measured as the CV. As in the original
247 analyses, all channels were statistically compared against each other. We then determined the median of
248 the effect size of comparisons across areas (i.e. the median effect size of the upper-right quadrant of the
249 comparison matrices in **Figs. 5, 6**; effect sizes of non-significant comparisons were set to 0), and plotted
250 this median against parameter combinations (**Figs. 7**) to determine how changing detection parameters
251 affected the reported inter-areal differences.

252 Burst co-occurrence analysis

253 The relationship between the onset of a burst in a specific channel and the cumulative burst co-
254 occurrence with all other channels was calculated as follows. First, given a certain channel (e.g. channel
255 A, for convenience) we determined the onset of all bursts detected across all recordings (the data from
256 the two bats were pooled given that spectral and bursting patterns were highly consistent across
257 animals). In a time window centred on each burst (spanning from -1000 to 1000 ms for delta frequencies,
258 and from -250 to 250 ms for the gamma frequencies) we counted and accumulated, for every channel,
259 the time points at which bursts occurred. Bursts were counted even if their onset or offset were outside
260 the aforementioned window, as long as at least a segment of the burst occurred within that window. For
261 every given channel (channel A in this example) this procedure yielded a matrix (dimensions: [channels x
262 samples]) whose values indicate the accumulated, co-occurring bursting activity in each other electrode,
263 relative to the times in which a burst onset occurred in the channel of interest (i.e. A in this case). We
264 referred to this matrix as a channel's burst co-occurrence matrix. Burst co-occurrence matrices were
265 computed for 8 channels, 4 in the FAF and 4 in the AC (at depths of 50, 250, 450, and 700 μm). This
266 reduced computational costs and facilitated visualization, while at the same time allowing to explore burst
267 co-occurrences at various depths in each region including superficial, middle and deep layers of cortex.

268 In order to evaluate whether the onset of a burst in a given electrode was related to the occurrence of
269 bursts in other electrodes, the burst co-occurrence matrix for the channel of interest (e.g. channel A) was
270 normalized following a bootstrapping procedure. We calculated 500 bootstrap burst co-occurrence
271 matrices, but instead of utilizing burst onsets as a reference, pseudo-random time points were used.
272 Because the accumulated number of co-occurring bursts across channels depends on the number of
273 burst onsets used from the reference channel (A), we ensured that the number of randomized time points
274 was equal to the number of burst onsets individually for each recording. The 500 pseudo-random burst
275 co-occurrence matrices were used as a baseline distribution, and the values of the burst co-occurrence
276 matrix for the channel of interest A were then Z-normalized relative to the bootstrap matrices. Absolute Z-
277 score values ≥ 6 were considered significant. Note that the Bonferroni correction of an alpha of 0.05 over
278 32 channels, 2 frequency bands, 8 channels of interest and 1000 time points yields a significance
279 threshold of 9.7×10^{-8} , equivalent to a Z-score of 5.2. In our analysis, negative Z-scores indicate a
280 suppression of burst activity relative to baseline, while positive values indicate an enhancement. These
281 procedures are illustrated in **Fig. 4A**.

282 A conceptual model of spike correlations and LFP waveform shape

283 Synthetic spike trains were modelled as inhomogeneous Poisson processes with firing rates controlled by
284 a pulse train with a frequency of 3 Hz. The duty cycle of the pulse train defines a temporal window in
285 which spiking occurs. Narrow spiking windows (i.e. lower duty cycles) constrain the firing of a neural
286 population in time, resulting in increased temporal correlations across neurons. By contrast, wider spiking

287 windows (i.e. higher duty cycles) result in decreased temporal spiking correlations across neurons. By
288 systematically adjusting the duty cycles we were therefore able to explore how temporal correlations in a
289 neuronal population (N = 30 neurons in our model) might affect LFP waveform shape.

290 From the spiking activity we derived synthetic LFP signals as follows. The spike train of each simulated
291 neuron was convoluted with a synaptic kernel whose rise and decay times were set to 1 and 20 ms,
292 respectively (function *sim_synaptic_kernel* of the python package NeuroDSP, version 2.2.1; (Cole et al.,
293 2019)). The sum of all convolutions was taken as the LFP signal. The procedure is illustrated in **Fig. 8A**.
294 We generated 300 s of spikes and LFPs for several values of duty cycles (5% to 60%, step: 5%). Cycle
295 features were extracted from the synthetic LFPs by applying of the *bycycle* algorithm described above.

296 Spike-spike correlations

297 All detected spiking events (see above) were included to calculate spike train correlations across
298 channels. Spike trains were binned using 5 ms bins, and the Pearson's correlation coefficient across pairs
299 of binned spike trains was computed using the *Elephant* toolbox (v. 0.12.0;
300 <https://github.com/NeuralEnsemble/elephant>). Correlation coefficients from channels located in the FAF
301 were averaged, and the same was done for channels located in the AC. This yielded one correlation
302 value per recording in FAF and AC, which allowed to capitalize on simultaneous recordings in both
303 regions by means of paired statistical comparisons (Wilcoxon signed-rank test, alpha = 0.05).

304 Pairwise phase consistency

305 The pairwise phase consistency (PPC) was computed as described in previous literature (Vinck et al.,
306 2010). Only spikes that occurred within oscillatory bursts in FAF or AC were considered. If more than
307 10000 spikes were detected in a given trace, 10000 spikes were randomly selected to calculate PPC
308 given that analyses were computationally expensive for large spike counts. In order to minimize the risk of
309 asymmetric signals yielding unclear measurements of phase, spike phases were not obtained by means
310 of a Hilbert transform or a Fourier analysis. Instead, the timing of a spike was expressed as the time in
311 which the event occurred relative the onset and offset of a cycle as detected in the time series by the
312 *bycycle* algorithm. Thus, each spike timing was between 0 and 1 (0 being the beginning of a burst cycle,
313 1 being the end), and was converted to a phase by multiplication with 2π . These phases were then used
314 for PPC calculation, which can be expressed as follows (Vinck et al., 2010):

$$315 \quad PPC = \frac{2}{N(N-1)} \sum_{j=1}^{N-1} \sum_{k=(j+1)}^N f(\phi_j, \phi_k), \quad [2]$$

316 where N is the number of spikes, and ϕ_j, ϕ_k represent the phases of spikes j and k , respectively. The
317 function $f(\phi_j, \phi_k)$ calculates the dot product between two unit vectors. It can be expressed as follows:

$$318 \quad f(\phi_j, \phi_k) = \cos(\phi_j) \cos(\phi_k) + \sin(\phi_j) \sin(\phi_k) \quad [3]$$

319 PPC values were averaged in FAF and AC, and paired statistical comparisons were made to evaluate
320 whether significant differences in spike phase consistency existed between regions (Wilcoxon signed-
321 rank test, $\alpha = 0.05$).

322 Statistical analyses

323 All statistical analyses were performed using *scipy* (version 1.9.1), or custom written Python scripts. For
324 determining significant deviations from a $1/f$ fitted trend in the LFP spectra one-sample t-tests were
325 performed. Statistical comparisons of median and CV values across regions (and within regions) were
326 performed using paired statistics (Wilcoxon signed-rank tests, $\alpha = 0.05$), as recordings in FAF and AC
327 were performed simultaneously ($N = 29$). Comparisons of spike-spike and spike-LFP correlation (PPC
328 values) were also made using paired statistics. Comparisons of burst lengths were made by means of
329 non-paired statistics (Wilcoxon rank-sum tests, $\alpha = 0.05$). All tests were corrected for multiple
330 comparisons using the false discovery rate when appropriate (Benjaminin and Hochberg procedure
331 (Benjamini and Hochberg, 1995)); it is noted in the main text whenever this correction was applied.

332 **Results**

333 Spectral properties of frontal and auditory cortical LFPs

334 A total of 29 paired recordings (i.e. simultaneous electrophysiological acquisition from each region) in
335 FAF and AC were performed in two bats: Bat-01 and Bat-02 ($N = 15$ and $N = 14$ paired FAF-AC
336 recordings, respectively). A schematic representation of the laminar probes, channel depths, and
337 recording locations in the AC are given in **Fig. 1A**. Since a clear map of the FAF does not exist, it was not
338 possible to map electrode locations in the frontal structure in a similar manner. Example frontal and
339 auditory cortical LFP traces from both animals are given in **Fig. 1B, K**, across all recording depths.
340 Typically, LFPs exhibited clear rhythmicity in low and high frequencies in both cortical regions. Evidence
341 for rhythmic activity was clear in grand-average spectra obtained from all ~ 20 -min long LFP traces (**Fig.**
342 **1C, G, L, M**). Observable “bumps” in these spectra are interpretable as deviations from a $1/f$ power-law (a
343 property of aperiodic mesoscopic signals such as LFPs (Baranauskas et al., 2012)) and therefore suggest
344 the presence of oscillatory activity. We performed spectral parametrization by fitting $1/f$ curves to the
345 power spectral density of every LFP signal recorded (Donoghue et al., 2020) in order to confirm that such
346 spectral bumps were in fact significant deviations from an aperiodic spectrum. Representative
347 parametrized spectra are depicted in **Fig. 1D, H, M, Q**, corresponding to the full ~ 20 -min LFP traces from
348 which data in **Fig. 1B, K** were selected. The $1/f$ fit is shown in dashed blue lines. Deviations in the spectra
349 from the power-law trend were clear in both animals, particularly in the FAF. We tested whether such
350 deviations were consistently present in all recordings by normalizing the power spectrum of each LFP
351 trace ($N = 15$ in Bat-01, $N = 14$ in Bat-02, per channel) to their fitted $1/f$ function (**Fig. 1E, I, N, R**). Power
352 spectral values would hover around 0 in the absence of consistent deviations, but would be significantly

353 above zero otherwise. Normalized spectral values were significantly above 0 in FAF and AC for both
354 animals (FDR-corrected one-sample t-tests; $p_{\text{corr}} < 1.73 \times 10^{-4}$, $t > 2.25$) at relatively low (~ 1 –5 Hz in FAF
355 and AC), intermediate (~ 12 –27 Hz in AC), and relatively high (ranging from ~ 32 –105 Hz, but peaking at
356 70–85 Hz in FAF and AC) frequencies (**Fig. 1F, J, O, S**).

357 In bats such as *C. perspicillata* (the animal studied here), LFP activity in low and high frequencies is
358 related to vocal production (e.g. at frequencies delta: 1–4 Hz, beta: 12–30 Hz, and gamma: 60–120 Hz;
359 see Garcia-Rosales et al. (2022b); Weineck et al. (2020)). Considering the above and the patterns of
360 deviations from a pure $1/f$ signal shown in **Fig. 1**, in subsequent analyses we focused on frequency bands
361 delta (1–4 Hz) and gamma (65–85 Hz). Beta-band frequencies were not included because no clear peaks
362 in this range were detected in FAF signals (**Fig. 1F, J, O, S**).

363 Cycle-by-cycle analysis of oscillatory activity in frontal and auditory cortices

364 To study the characteristics of delta- and gamma-band rhythmic activity in frontal and auditory areas, we
365 performed a cycle-by-cycle analysis of the recorded LFP. Cycles were considered only if they were part of
366 consistent oscillatory activity (i.e. they were associated with a putative oscillatory bursts). Bursts of
367 oscillatory activity were detected using the *bycycle* algorithm (Cole and Voytek, 2019), which capitalizes
368 on a time-domain approach for quantifying waveform shape (**Fig. 2A**). A burst is detected based on four
369 parameters, which control for signal-to-noise ratio (SNR) and waveform consistency (see Methods). In
370 this context, an oscillatory burst occurs if the threshold values of these parameters are exceeded for at
371 least 3 consecutive cycles.

372 Representative burst events in delta- and gamma-bands are shown for FAF and AC in **Fig. 2B**. The
373 waveform shape of oscillatory activity was quantified by measuring three main features on a cycle-by-
374 cycle basis: cycle period, cycle rise-decay asymmetry, and cycle peak-trough asymmetry (**Fig. 2C**; Cole
375 and Voytek (2019)). For each LFP trace, the median feature value across all detected cycles was
376 considered the waveform shape feature for that trace (**Fig. 2D**). The median summarizes a distribution of
377 feature values, yielding one value per LFP trace (that is, 29 values for each FAF and AC channel). The
378 median feature value of asymmetry metrics was normalized to 0.5 to account for possible confounds
379 related to signal polarity differences in FAF and AC (see Methods; (Schaworonkow and Voytek, 2021)).
380 To determine how and to what extent oscillatory waveform shape differed between recording locations,
381 we performed systematic channel-by-channel pairwise comparisons. Only values obtained from
382 simultaneously recorded LFP traces were compared to one another by using paired statistical testing.
383 Median values for each ~ 20 -minute LFP were quantified from hundreds of cycles. That is, for Bat-01, no
384 less than 665 and 370 delta-band cycles were used from FAF and AC, respectively, while no less than
385 829 and 146 gamma-band cycles were used from the same regions. For Bat-02, at least 561 and 468
386 delta-band cycles were used from FAF and AC, while at least 717 and 241 gamma-band cycles were
387 used from the same areas.

388 Bursting dynamics in frontal and auditory cortices

389 The data shown in **Fig. 1** suggest that the signal-to-noise ratio (SNR) of oscillatory activity in delta- and
390 gamma bands is higher in FAF than in AC. We quantified SNR independently for each bat in frontal and
391 auditory regions on a channel-by-channel basis (N = 15 observations for each channel in FAF or AC for
392 Bat-01, and N = 14 for Bat-02). Distribution of SNR values are shown in **Fig. 3B** (top) for delta
393 frequencies and in **Fig. 3E** (top) for gamma frequencies. Distributions from Bat-01 are shown with positive
394 probability densities, whereas data from Bat-02 are given with negative probability densities merely for
395 illustrative purposes. Note that the colour of each distribution corresponds to a specific channel in the
396 shank, located at a certain cortical depth (see **Fig. 3A**). Given that the patterns across animals were
397 highly consistent, we compared SNR values across recording sites by pooling data from the two bats.
398 Channel-by-channel statistical comparisons revealed significant differences in SNR across recording sites
399 (FDR-corrected Wilcoxon signed-rank tests, N = 29, significance when $p_{\text{corr}} < 0.05$). Comparisons are
400 summarized in the matrices of **Fig. 3B-G** (bottom). A comparison matrix represents the effect sizes (d) of
401 pairwise comparisons of SNR values across channels ($|d| < 0.5$ small, $0.5 \leq |d| \leq 0.8$ medium, $|d| > 0.8$
402 large effect sizes; Cohen (2013)). A cell (r, c) in a matrix shows the effect size of comparing SNRs from a
403 channel indexed by row r, and a channel indexed by column c (i.e. channel r vs. channel c). The
404 relationship between a channel index and its relative depth in frontal or auditory cortex is schematized in
405 **Fig. 3A** (notice the vertical lines next to channel numbers in **Fig. 3B-G** indicating cortical depths by
406 following the colour schemes of **Fig. 1** and **Fig. 3A**). The upper right quadrant of each matrix represents
407 comparisons of channels in FAF vs. those in AC. Only effect size values of significant comparisons ($p_{\text{corr}} <$
408 0.05) were shown; they were set to 0 otherwise. The matrices in **Fig. 3B** and **Fig. 3E** show strong
409 differences in SNR between frontal and auditory cortices in the delta and gamma bands.

410 Typically, SNR values are interpreted solely on the basis of signal amplitude. However, high SNRs
411 derived from the spectral properties of a signal could also indicate, beyond amplitude, a relatively high
412 proportion of oscillatory events. We calculated bursting proportion as the ratio of the total time of bursting
413 in an LFP trace relative to the total duration of that trace. Distribution of bursting proportions are given for
414 both animals in **Fig. 3C** (top) for delta frequencies and in **Fig. 3F** (top) for gamma frequencies. From
415 these data it appeared clear that, in both animals, the proportion of bursting events in FAF was higher
416 than that in AC. Given this consistency, we pooled data across bats and compared on channel-by-
417 channel basis bursting proportions across sites (FDR-corrected Wilcoxon signed-rank tests, N = 29,
418 significance when $p_{\text{corr}} < 0.05$). These comparisons, summarized in the matrices of **Fig. 3C** (bottom) and
419 **Fig. 3F** (bottom), corroborate that the proportion of delta- and gamma-band oscillatory events was
420 significantly higher in FAF than in AC, with large effect sizes.

421 Higher proportion of bursting events could be influenced by two factors: more bursts occur in FAF than in
422 AC, or bursts in FAF are longer than those in the auditory cortex (or both). To elucidate this, we examined

423 the distributions of burst durations in delta- and gamma-band LFP traces from all channels. Distribution of
424 burst durations are given independently for each animal in **Fig. 3D** (top) for delta and **Fig. 3G** (top) for
425 gamma frequencies. To statistically compare burst durations, data across bats were pooled given the
426 highly similar patterns observed from the two animals. For comparisons, all bursts from any given channel
427 are considered, so the number of bursts per channel was not always the same (at least 2283 and 1977
428 bursts were used for delta frequencies from Bat-01 and Bat-02, respectively; in gamma, no less than
429 2984 and 1991 for each bat). Because of the uneven burst counts, channel-by-channel comparisons were
430 not paired (FDR-corrected Wilcoxon ranksum tests, $N \geq 1991$, significance when $p_{\text{corr}} < 0.05$). As readily
431 visible from the distributions of burst duration, and as shown in the comparison matrices from **Fig. 3D**
432 (bottom) and **Fig. 3G** (top), differences in burst durations between FAF and AC were statistically
433 negligible, indicating that bursts in the FAF were more numerous, but not necessarily longer, than in the
434 AC. This corresponds well with our initial observation of a very large burst density in frontal regions.

435 The data shown in **Figs. 1** and **3** demonstrate that spectral and bursting dynamics were highly consistent
436 between Bat-01 and Bat02. Because of this consistency between animals (**Figs. 1** and **3**), data from the
437 two bats were pooled in subsequent analyses.

438 Bursting events in FAF and AC are temporally correlated

439 Transfer entropy analyses based on the phase of ongoing LFP activity, and direct electrical
440 microstimulation of the frontal cortex to alter AC responsiveness, show that neural activity in FAF can
441 significantly modulate its auditory cortical counterpart (Garcia-Rosales et al., 2022b). Given the functional
442 and anatomical connections in the FAF-AC network, we sought to determine whether oscillatory bursts in
443 one region are related to bursts occurring in the other. We reasoned that co-occurring bursts across brain
444 structures could be a fingerprint of functional connectivity complementary to phase correlations (e.g.
445 coherence), statistical dependencies (e.g. transfer entropy), or invasive approaches (e.g. electrical
446 microstimulation). We calculated the burst co-occurrence index (**Fig. 4**), a metric that quantifies for any
447 given channel the relationship between the onset of its own bursts with the occurrence of bursts in other
448 channels (**Fig. 4A** illustrates how the index was computed). The burst co-occurrence index is shown in
449 **Fig. 4B, C**, calculated for eight channels in total, four in each region, at representative depths of 50, 250,
450 450, 700 μm . Since the index is a cumulative count Z-normalized according to bootstrap distributions (see
451 Methods), we could use it to evaluate the significance of burst co-occurrence across channels. Thus, red
452 colours in **Fig. 4** indicate significant, temporally correlated increases in bursting activity in other channels
453 (Z -values ≥ 6), while blue colours indicate significant, temporally correlated suppression of bursting
454 activity in other channels (Z -values ≤ -6). White colours indicate no significant deviations from baseline
455 values.

456 At delta frequencies (**Fig. 4B**), a burst onset in either FAF or AC was typically preceded by a suppression
457 of bursting activity in channels of the same structure, and succeeded by a within-structure increase in

458 burst co-occurrence across channels, peaking as trivially expected in the channel from which burst onsets
459 were chosen. A similar pattern was observable for bursts detected in the gamma frequency range (**Fig.**
460 **4C**). However, we observed no clear pre-onset suppression in the gamma band, potentially due to much
461 shorter durations of gamma bursts compared to delta ones. In gamma frequencies, an interesting pattern
462 was evident: when burst onsets were taken from FAF channels (top left quadrant of **Fig. 4C**), a periodicity
463 of burst co-occurrence emerged in the frontal area, with a temporal scale of ~250 ms. This phenomenon
464 constitutes evidence for strong coupling between gamma-band activity and low-frequency (delta)
465 rhythms. These data resonate with that of a second study (and a different dataset) demonstrating clear
466 coupling between the amplitude of gamma-band and the phase of delta-band LFPs in the FAF of *C.*
467 *perspicillata* (Garcia-Rosales et al., 2022a).

468 Remarkably, when a burst onset occurred in frontal or auditory cortex, significant and consistent changes
469 in burst co-occurrence in the other region happened for gamma-band LFPs (**Fig. 4C**). That is, bursts
470 onsets in FAF were consistently and significantly correlated with gamma-band bursting in the AC, and
471 vice-versa. Furthermore, **Fig. 4C** suggests a degree of spatial specificity to this relationship, wherein
472 bursts originating in FAF appear more strongly related to those in middle layers of the AC (depths of 250-
473 450 μm), while bursts originating in middle layers of the AC yield larger co-activation patterns in the FAF.
474 Significant inter-areal burst co-occurrence was not equally clear in delta frequencies (**Fig. 4B**), although
475 clear FAF-AC interactions occur in the delta band when considering transfer entropy analysis or even
476 electrical stimulation experiments (Garcia-Rosales et al., 2022b). The apparent lack of burst interactions
477 in the delta band shown in **Fig. 4B**, however, does not necessarily mean the absence of burst co-
478 occurrence in these frequencies. Rather, this effect is a consequence of the stringency of the
479 bootstrapping procedure (see Methods) interacting with the ubiquity of bursting activity in the FAF (**Fig.**
480 **3**). That is, bootstrap distributions were contaminated with real bursting activity when accumulating burst
481 counts from the frontal cortex. Taken together, these results (particularly the ones related to gamma-band
482 LFPs) suggest an intrinsic relationship between elevated bursting activity in frontal and auditory cortices,
483 supporting the notion of strong functional connectivity in the FAF-AC network.

484 Oscillatory waveform shape differences between frontal auditory cortices

485 We have shown the presence of oscillatory activity in delta and gamma frequencies in the frontal and
486 auditory cortices of *C. perspicillata*. Oscillatory bursts across structures occur more often in the FAF, but
487 are not necessarily longer than those in the AC. Remarkably, bursts in FAF and AC are temporally
488 correlated, supporting the notion of concerted activity in the delta and gamma ranges in the FAF-AC
489 circuit. Such correlated bursting activity occurs in very similar frequencies, yet they occur in functionally
490 and anatomically distinct areas of the brain. Do these oscillations differ across structures?

491 A visual inspection of ongoing LFP activity revealed that the oscillatory waveform in the FAF was highly
492 asymmetric (i.e. less sinusoidal, with more pronounced troughs), something that was not so obvious in

493 the AC (see, for example, the representative bursts in **Fig. 2B**). The waveform shape of an oscillation was
494 characterized by three main features (see above): period, rise-decay asymmetry, and peak-trough
495 asymmetry. The distribution of feature values across recordings is given in **Fig. 5B-D** (top) for delta
496 frequencies, and in **3E-G** (top) for gamma frequencies for all channels (see **Fig. 5A**; conventions are the
497 same used for presenting data in **Fig. 3**). Note that the median feature value across all cycles is
498 considered the feature value for a given LFP trace (**Fig. 2D**), thus yielding 29 feature values for each
499 electrode either in FAF or AC (i.e. one value per recording). This allowed us to compare between
500 recording sites using paired statistics, capitalizing on the fact that data in FAF and AC were
501 simultaneously acquired.

502 Channel-by-channel comparisons revealed significant differences across cortical regions (FDR-corrected
503 Wilcoxon signed-rank tests, significance when $p_{\text{corr}} < 0.05$). These analyses are summarized in the
504 comparison matrices of **Fig. 5B-G** (bottom; conventions are the same as those of **Fig. 3**). Delta-band
505 oscillations in frontal and auditory cortices differed in period typically with small-to-medium effect sizes ($|d|$
506 ≤ 0.8 ; **Fig. 5B**, bottom), but were strongly different in terms of their temporal asymmetries (**Fig. 5C-D**,
507 bottom; $|d| > 0.8$ particularly for peak-trough asymmetries). The data in **Fig. 5** corroborates that the
508 differences visible in **Fig. 2B** were consistent across recordings. Regarding gamma-band LFPs, the
509 period of gamma-band cycles in FAF and AC differed more markedly than that of delta-band cycles (**Fig.**
510 **3E**, bottom; $|d| > 0.8$), although gamma-band oscillations differed only negligibly in their asymmetry
511 across structures.

512 Waveform shape variability is higher in auditory than in frontal cortex

513 By examining recordings independently we observed that beyond direct differences in waveform shape
514 features (or lack thereof), feature values across cycles were typically less variable in the FAF than in the
515 AC. That is, the distribution of feature values (e.g. period) were typically narrower for LFPs recorded in
516 the frontal cortex. To evaluate the extent of this effect, we quantified for each LFP trace the variability of
517 waveform shape features as the coefficient of variation (CV; **Fig. 2D**), and compared it across recording
518 sites. The CV is a measure of dispersion, in the sense that it measures the “broadness” of a distribution.
519 Thus, larger CVs indicate that cycle features vary over a wider range of possible values, suggesting a
520 higher variability in the oscillatory processes. As with the median, the CV summarizes a distribution,
521 yielding one value per LFP trace (see above and **Fig. 2D**). The same cycles used to calculate median
522 feature values were used to calculate CV values.

523 The distributions of CV values across cycle features for each channel are given in **Fig. 6B-D** (top) for
524 delta frequencies, and **Fig. 6E-G** (top) for gamma frequencies. CV values appeared consistently lower for
525 channels in FAF than for those in AC. This trend was confirmed by statistical, channel-by-channel
526 pairwise comparisons (FDR-correct Wilcoxon signed-rank tests, $N = 29$, significance when $p_{\text{corr}} < 0.05$),
527 summarized in comparison matrices similar to those of **Fig. 3**. Statistical comparisons between channels

528 located in different regions (the upper right quadrants of the comparison matrices) yielded the highest
529 effect sizes (typically $|d| > 0.8$, large). CV values were consistently and significantly lower in FAF channels
530 than in AC channels, in delta- and gamma frequency bands, for all cycle features. Some significant
531 within-area differences also occurred (e.g. deeper channels in FAF had higher CV values than more
532 superficial ones), yet effect sizes were typically medium ($0.5 < |d| < 0.8$) or small ($|d| < 0.5$). Overall, these
533 results indicate that, beyond first-order differences in waveform shape, oscillatory activity in the frontal
534 cortex exhibits a higher degree of cycle-by-cycle regularity (i.e. lower variability over cycles) than that of
535 the AC. Note that such differences in regularity between regions are unlikely to arise from differences in
536 the bursting proportions across FAF and AC (**Fig. 3**). Although more bursts result in more cycles
537 contributing to a distribution, cycle-by-cycle regularity is quantified here using hundreds (sometimes
538 thousands) of cycles obtained from relatively long LFP traces (ca. 20 minutes). These are well-sampled
539 distributions whose CV should not be strongly affected by increasing the number of waveform shape
540 features in them.

541 Differences across regions are robust against burst detection parameters

542 The data indicate that oscillations in the FAF are more regular than those in the AC. However, the
543 measurements of waveform shape used here can be affected by the SNR of the oscillatory activity used
544 to quantify them. In particular, higher SNR of oscillatory activity in FAF (**Fig. 3B**) could result in narrower
545 distributions of cycle features, because low SNR increases the variability of waveform shape features
546 (see Schaworonkow and Nikulin (2019)). The SNR for burst detection is controlled by the parameter
547 amplitude fraction threshold, which discards cycles below a certain amplitude percentile calculated from
548 all cycles in an LFP trace (Cole and Voytek, 2019; Schaworonkow and Voytek, 2021). Therefore, to test
549 whether the results shown above can be simply accounted for by different SNR levels in FAF and AC, we
550 evaluated the sensitivity of the inter-areal differences to different values of amplitude fraction threshold in
551 each region (**Fig. 7**).

552 The median effect size of inter-areal comparisons was used as a summary metric of differences in
553 median feature values (**Fig. 7A, B**) and CV values (**Fig. 7C, D**) across cortical regions. This metric
554 corresponds to the median value of the upper-right quadrant of the comparison matrices in **Figs. 5** and **6**.
555 We systematically varied the amplitude fraction threshold parameter (range: 0.1 – 0.9, step of 0.1) used
556 to detect oscillatory bursts independently in the FAF or the AC, and for each iteration we calculated the
557 median effect size of inter-areal comparisons. As depicted in **Fig. 7A**, period values for delta-band cycles
558 were different between FAF and AC with typically medium or even low effect sizes ($|d| < 0.5$ for low, 0.5
559 $\leq |d| < 0.8$ for medium), while asymmetries differed with typically strong effect sizes ($|d| > 0.8$)
560 particularly when considering the peak-trough asymmetry as in **Fig. 5**. In general, observations across a
561 broad range of threshold values conformed well to the data depicted in **Fig. 5** in delta- and gamma-bands
562 (**Fig. 7B** for gamma). Those data were obtained with a threshold value of 0.5 (red squares in **Fig. 7**).
563 Similarly, CVs were consistently lower in FAF than in AC across a wide range of amplitude fraction

564 threshold values in both delta- and gamma frequencies (**Fig. 7C**, delta; **Fig. 7D**, gamma), for all three
565 cycle features considered. These data were highly consistent with those shown in **Fig. 6**. These results
566 indicate that the differences in waveform shape features and their CV values between frontal and auditory
567 cortices are not trivially accounted for by differences in SNR across regions.

568 A conceptual model captures patterns of waveform shape differences between FAF and AC

569 We hypothesized that differences across areas, particularly when considering the CV of waveform
570 features, might reflect the activity of two distinct cortical generators exhibiting different degrees of
571 regularity. We illustrate this idea with a conceptual model in which an oscillation occurs as a consequence
572 of the temporally aligned rhythmic discharge of a population of neurons. This conceptualization makes no
573 assumption on the nature of the neuronal oscillators themselves (see Discussion); instead, it only
574 assumes that extracellular oscillatory activity occurs when a sufficiently large neuronal population fires
575 concertedly (Buzsaki et al., 2012). We reasoned that a highly synchronous population firing would lead to
576 a strong current at a specific phase of the LFP resulting in relatively asymmetric waveform shapes; by
577 contrast, a relatively asynchronous population activity would yield less asymmetric temporal features. We
578 simulated 30 neurons firing rhythmically for 300 seconds at a delta rate (3 Hz, for illustrative purposes;
579 this can be generalized to other frequencies as well), with varying degrees of synchronicity among them.
580 The synchronization of the spiking across neurons was manipulated by changing the duty cycle of a
581 square pulse train determining to the instantaneous rate of an inhomogeneous Poisson process
582 controlling a neuron's firing rate (see Methods). Lower duty cycles represent narrower spiking windows
583 and therefore higher synchronicity across neurons. From the neuronal firing in each condition, we
584 generated a synthetic LFP by convoluting each spike train with a synaptic kernel and adding them over all
585 neurons (**Fig. 8A**). This synthetic LFP was used to estimate cycle features computed with the *bicycle*
586 algorithm, analogue to the analyses performed on the empirical data.

587 Simulated spiking activity with various degrees of synchronicity (controlled by the duty cycle parameter) is
588 shown in **Fig. 8B** together with corresponding LFPs. Figure **8C-E** shows the distribution of cycle features
589 (**Fig. 8C**, period; **Fig. 8D**, rise-decay asymmetry; **Fig. 8E**, peak-trough asymmetry) for each duty cycle
590 condition. We did not observe changes in the median period across duty cycles. However, we did
591 observe a consistent change in temporal asymmetries (**Fig. 8D, E**) indicating that a more synchronous
592 neuronal population (lower duty cycles in the figure) resulted in more asymmetric waveform shapes. Note
593 that the farther the median feature value is from 0.5 (black line in **Fig. 8D, E**) the more asymmetric LFP
594 cycles are. In addition, we observed that as the neuronal population became less synchronized (i.e.
595 higher duty cycles) feature values became more variable, as illustrated by the fact that the CV obtained
596 from the feature distributions tended to increase together with the duty cycle (**Fig. 8G-H**). These two
597 cases (higher asymmetry for more synchronized population spiking and more variability for less
598 synchronized spiking) reflect differences in delta- and gamma-band oscillations in FAF and AC (i.e. higher

599 asymmetry and less variability for oscillations in FAF), and offer a simple yet plausible account of the
600 patterns observed across regions.

601 These results suggest that differences in FAF and AC waveform shape can at least be partially accounted
602 for by different degrees of synchronicity in the underlying neuronal firing. To test this prediction, we turned
603 to the spiking activity in frontal and auditory regions (**Fig. 9A**). Since oscillations were more asymmetric
604 and less variable in FAF, we hypothesized that neuronal spiking would be more highly correlated in
605 frontal than in auditory cortex and, additionally, more strongly synchronized with LFP oscillations (a
606 secondary consequence of the model in **Fig. 8**). For each recording, we averaged correlation coefficients
607 obtained from FAF and AC channels, and tested whether their values were significantly different across
608 regions. These analyses corroborated that spike train correlations were higher in frontal regions (**Fig. 9B**,
609 bottom; Wilcoxon signed-rank test, $p = 2 \times 10^{-6}$) with a large effect size ($d = 0.84$).

610 Because delta-band oscillations exhibited the largest differences in terms of asymmetry (**Fig. 5**), we
611 studied spike-LFP relationships in this frequency range. Here, only spikes occurring within oscillatory
612 bursts, as detected by the *bycycle* algorithm, were considered (note that these are the same bursts used
613 in previous analyses). Spike times were expressed as the points of spike occurrence relative to the period
614 of the burst cycle in which they occurred (0, spike occurs at beginning of cycle; 1, spike occurs at end of
615 cycle), and spike phases were obtained by multiplying the relative spike timing by 2π . The distribution of
616 spike phases from the recordings shown in **Fig. 9A** are depicted in **Fig. 9C** ($N = 6760$ spikes in FAF, $N =$
617 661 spikes in AC), suggesting a tighter clustering of spike phases in FAF. The pairwise phase
618 consistency (PPC; Vinck et al. (2010)) was computed for all channels across recordings. The PPC
619 measures how tightly spike phases group together (phase consistency) and constitutes a bias-free
620 equivalent to the square of the phase locking value. Higher PPC values indicate higher spike-LFP
621 coherence. To test whether spikes in FAF were more strongly synchronized to delta-band LFPs than
622 those in the AC, we averaged PPC values across channels in FAF and AC (as described above) and
623 statistically compared across regions. PPC values were significantly higher in FAF than in AC (**Fig. 9D**,
624 bottom; Wilcoxon signed-rank test, $p = 9.75 \times 10^{-4}$) with a large effect size ($d = 0.96$).

625 Altogether, these results show that differences in waveform asymmetries between FAF and AC in delta
626 frequencies are accompanied by differences in spike correlations and spike-LFP synchronization between
627 regions. These observations are in line with predictions derived from the conceptual model illustrated in
628 **Fig. 8**, and support a relationship between waveform shape and spike synchronization. Direct correlations
629 between, for example, peak-trough asymmetry and spike-train correlations were, although significant,
630 relatively weak (FAF, $p = 0.033$, adjusted $R^2 = 0.13$; AC, $p = 0.009$, adjusted $R^2 = 0.2$), indicating that
631 oscillatory waveform shape cannot be trivially explained by local spike synchronization alone.

632 **Discussion**

633 In this work, oscillations in the bat frontal and auditory cortices were studied with respect to their
634 waveform shape. We show that oscillations present in simultaneously recorded LFPs in the fronto-
635 auditory circuit differ markedly in waveform shape and in the variability of waveform features across
636 individual cycles. This heterogeneity is not trivially accounted for by different levels of SNR in frontal and
637 auditory regions. A conceptual model suggests a relationship between the temporal organization of
638 neuronal spiking and waveform shape asymmetry, with higher spike temporal correlations leading to
639 more asymmetric waveforms. In line with the predictions of the model, we demonstrate that spike-spike
640 and spike-LFP correlations differ significantly in the FAF-AC network.

641 The bat frontal and auditory cortices are two brain regions with distinct cytoarchitectonic patterns, which
642 likely accounts for the differences observed in oscillatory waveform shape across areas. *C. perspicillata*'s
643 AC is a primary sensory region with a well-defined, six-layered columnar structure and clear inter-laminar
644 boundaries (see Garcia-Rosales et al. (2019) for histology), following a blueprint that is typical across
645 mammalian species (Douglas and Martin, 2004; Linden and Schreiner, 2003; Mountcastle, 1997). By
646 contrast, *C. perspicillata*'s FAF lacks clear boundaries between layers (see Garcia-Rosales et al. (2022b);
647 Weineck et al. (2020)), mirroring instead the stereotypical agranular or slightly agranular architecture of
648 the mammalian frontal cortex (Beul and Hilgetag, 2014; Camarda and Bonavita, 1985; Shepherd, 2009).
649 Differences between the bat frontal and auditory regions likely extend to other cytoarchitectonic properties
650 such as the distribution of cell-type density and overall cellular organization. Beyond anatomy, cortical
651 cytoarchitecture plays a significant role in defining activity patterns and brain function. Indeed, the
652 functional characteristics of a given region are well-related to its cytoarchitecture (Badre and D'Esposito,
653 2009; Pandya and Yeterian, 1996), which includes the nature of incoming and outgoing axonal
654 connections (Hilgetag et al., 2019; Kritzer et al., 1992; Passingham et al., 2002), cell-type specific
655 characteristics (e.g. density, morphology; Benavides-Piccione et al. (2002); Beul and Hilgetag (2014)),
656 and laminar organization (Hooks et al., 2011). Local cytoarchitecture affects neuronal firing patterns,
657 which are known to vary consistently across functionally and anatomically well-defined regions (Badre
658 and D'Esposito, 2009; Mochizuki et al., 2016; Shinomoto et al., 2009). Anatomical differences between
659 granular and agranular cortical areas also result in distinct intra- and inter-laminar connectivity patterns
660 (Beul and Hilgetag, 2014; Shepherd, 2009), which may also affect the dynamics of the generators of
661 cortical oscillatory activity. Together, local anatomy, spiking patterns, and connectivity influence
662 mesoscopic measurements of activity such as LFPs or other signals recorded non-invasively (Buzsaki et
663 al., 2012; Cole and Voytek, 2017).

664 Other than local cytoarchitecture, respiration can also affect both single-neuron and oscillatory activities
665 (Tort et al., 2018). For example, respiratory rhythms in mice entrain single neuron spiking and local
666 cortical oscillations particularly –but not only- in frontal regions, (Koszeghy et al., 2018; Tort et al., 2018)

667 with measurable functional consequences (Bagur et al., 2021; Folschweiller and Sauer, 2023). Likewise,
668 heart rate fluctuations are known to correlate with brain oscillations, particularly during sleep (Mara and
669 Julian, 2018; Mikutta et al., 2022). Respiratory or cardiac rhythms were not measured in this study, but
670 their potential effects cannot be directly ruled out given that typical values for *C. perspicillata* lie close to
671 delta frequencies: respiration rate, ~2.5–4.5 Hz; hear rate: ~8.33 Hz. For example, it is possible that
672 respiration influences the patterns of rhythmicity and asymmetry overserved in frontal areas by directly
673 modulating the LFP, by synchronizing neuronal spiking (thereby altering the LFPs), or a combination of
674 both. Future studies should clarify the roles –if any- of respiration or heart rate in modifying oscillatory
675 waveform shape dynamics.

676 Delta-band oscillations differed markedly across regions in terms of their temporal asymmetries,
677 something that did not occur consistently for gamma-band activity (**Fig. 5**). However, for both frequency
678 ranges we observed large and consistent inter-areal differences in the variability of shape feature values
679 across individual cycles (**Fig. 6**). A conceptual model (**Fig. 8**) suggests that temporal asymmetries (i.e.
680 waveform shape features) and their variability across cycles, could depend on the degree of correlated
681 activity of the underlying neuronal population. The model in **Fig. 8** suggests that more synchronous
682 populations yield highly asymmetric waveform shape and lower cycle-by-cycle variability, while less
683 synchronous populations yield gradually a more sinusoidal shape with more variable cycle-by-cycle
684 features. That waveforms become less asymmetric can be explained by temporal averaging of the
685 contribution of each spike to the LFP, akin to the expected effects of spatial averaging in electro- or
686 magneto-encephalographic recordings (Schaworonkow and Nikulin, 2019). Note that the model does not
687 make any assumptions about important features of the underlying generators, such as location in the
688 local circuitry, connectivity patterns, or component cell-types. As discussed above, these factors can
689 influence both waveform shape and spiking dynamics. Instead, the model provides a parsimonious
690 account of the empirical data shown in **Fig. 5**, assuming only that spiking is an important contributor to
691 the LFP (Buzsaki et al., 2012). The model in **Fig. 8**, together with the waveform shape differences across
692 regions, affords one prediction, namely that spike-spike and spike-LFP correlations should be higher in
693 the area with more asymmetric signals (i.e. the FAF). Our results in **Fig. 9** corroborate such prediction,
694 illustrating that the bat frontal cortex exhibits more correlated spiking, which is also more strongly
695 synchronized the ongoing LFP phase in delta frequencies. As a concept, and supported by our data, the
696 model draws a relationship between waveform shape asymmetry and the temporal dynamics of neuronal
697 spiking in the neocortex.

698 A hypothesis stemming from the above observations is that differences in the variability of cycle features
699 (measured by the CV) between FAF and AC might be explained by different values of temporal
700 correlations in the underlying generators. In other words, it could be speculated that putative generators
701 in the FAF operate with tighter parameters (reflected in higher temporal correlations) than their AC
702 counterparts. One possible take on the functional implications of such phenomenon would be that frontal

703 circuits rely more on internal timescales, while auditory circuits exhibit an elevated flexibility and
704 perturbability. Previous studies have demonstrated that activity patterns in the rodent prefrontal cortex
705 exhibit less variability than those of sensory regions (Castano-Prat et al., 2017; Ruiz-Mejias et al., 2011),
706 potentially reflecting a cortical hierarchy of excitability and circuit properties. In such hierarchy, peripheral
707 areas exhibit more adaptability to sensory stimuli (and therefore more variability), while frontal areas
708 exhibit higher stimulus independence, yielding activity patterns better related to local network dynamics
709 (Badre and D'Esposito, 2009; Braun and Mattia, 2010; Ruiz-Mejias et al., 2011)). In the bat brain, the FAF
710 appears to be a modulation and control structure that may also be involved in the integration of diverse
711 inputs during echolocation and navigation, as reflected by its internal dynamics and by the anatomical
712 and functional connectivity patterns with other cortical and subcortical regions (Casseday et al., 1989;
713 Eiermann and Esser, 2000; Garcia-Rosales et al., 2022b; Kanwal et al., 2000; Kobler et al., 1987;
714 Weineck et al., 2020). Conversely, the bat AC (as that of other mammals) is primarily tasked with
715 representing sounds that may unfold in time over nested timescales, typically exhibiting varying degrees
716 of periodicity which require higher adaptability and flexibility (Doelling et al., 2019; Garcia-Rosales et al.,
717 2018; Henry and Obleser, 2012; Lakatos et al., 2013; Teng et al., 2017). Indeed, previous modelling work
718 suggests that neuronal response patterns in FAF and AC can be accounted for by slower synaptic
719 dynamics in the frontal region (Lopez-Jury et al., 2020), something that could be detrimental for precise
720 stimulus tracking but that could be important for sensory integration. From the above, we hypothesize that
721 a higher level of variability in the auditory cortical circuitry (**Fig. 6**) might aid with efficient sensory
722 representations in AC (see Pittman-Polletta et al. (2021)), while narrower dynamics could be important for
723 high-level computations in FAF (e.g. sensory integration), closely tied to internal timescales and more
724 robust against external perturbations.

725 In conclusion, we have shown that simultaneously recorded oscillatory activity across frontal and auditory
726 cortices differs markedly in waveform shape. Additionally, a conceptual model, paired with empirical
727 results, suggests a relationship between waveform shape and local spiking activity. This intriguing
728 relationship could serve as a tool for constraining generative models of neural oscillations, and can be
729 used to draw hypotheses after observing waveform shape differences across experimental conditions.
730 The oscillations studied here in frontal and auditory regions occur in similar frequencies and are
731 functionally related (**Fig. 4**; (Garcia-Rosales et al., 2022b)), but they nevertheless possess distinct
732 dynamics that reflect the heterogeneous anatomical and functional properties of the bat fronto-auditory
733 network.

734

735 **References**

736 Badre, D., and D'Esposito, M. (2009). Is the rostro-caudal axis of the frontal lobe hierarchical? *Nature*
737 *Reviews Neuroscience* 10, 659-669.

738 Bagur, S., Lefort, J.M., Lacroix, M.M., de Lavilleon, G., Herry, C., Chouvaeff, M., Billand, C., Geoffroy, H.,
739 and Benchenane, K. (2021). Breathing-driven prefrontal oscillations regulate maintenance of conditioned-
740 fear evoked freezing independently of initiation. *Nat Commun* 12, 2605.

741 Baranauskas, G., Maggiolini, E., Vato, A., Angotzi, G., Bonfanti, A., Zambra, G., Spinelli, A., and Fadiga,
742 L. (2012). Origins of $1/f^2$ scaling in the power spectrum of intracortical local field potential. *J Neurophysiol*
743 107, 984-994.

744 Benavides-Piccione, R., Ballesteros-Yanez, I., DeFelipe, J., and Yuste, R. (2002). Cortical area and
745 species differences in dendritic spine morphology. *J Neurocytol* 31, 337-346.

746 Benjamini, Y., and Hochberg, Y.J.J.o.t.R.s.s.B. (1995). Controlling the false discovery rate: a practical
747 and powerful approach to multiple testing. 57, 289-300.

748 Beul, S.F., and Hilgetag, C.C. (2014). Towards a "canonical" agranular cortical microcircuit. *Front*
749 *Neuroanat* 8, 165.

750 Braun, J., and Mattia, M. (2010). Attractors and noise: twin drivers of decisions and multistability.
751 *Neuroimage* 52, 740-751.

752 Buzsaki, G., Anastassiou, C.A., and Koch, C. (2012). The origin of extracellular fields and currents--EEG,
753 ECoG, LFP and spikes. *Nat Rev Neurosci* 13, 407-420.

754 Camarda, R.M., and Bonavita, V. (1985). The frontal agranular cortex and the organization of purposeful
755 movements. *Ital J Neurol Sci* 6, 287-315.

756 Casseday, J.H., Kobler, J.B., Isbey, S.F., and Covey, E. (1989). Central acoustic tract in an echolocating
757 bat: an extralemniscal auditory pathway to the thalamus. *J Comp Neurol* 287, 247-259.

758 Castano-Prat, P., Perez-Zabalza, M., Perez-Mendez, L., Escorihuela, R.M., and Sanchez-Vives, M.V.
759 (2017). Slow and Fast Neocortical Oscillations in the Senescence-Accelerated Mouse Model SAMP8.
760 *Front Aging Neurosci* 9, 141.

761 Cohen, J. (2013). *Statistical power analysis for the behavioral sciences* (Routledge).

762 Cole, S., Donoghue, T., Gao, R., and Voytek, B.J.J.o.O.S.S. (2019). NeuroDSP: a package for neural
763 digital signal processing. 4, 1272.

764 Cole, S., and Voytek, B. (2019). Cycle-by-cycle analysis of neural oscillations. *J Neurophysiol* 122, 849-
765 861.

766 Cole, S.R., van der Meij, R., Peterson, E.J., de Hemptinne, C., Starr, P.A., and Voytek, B. (2017).
767 Nonsinusoidal Beta Oscillations Reflect Cortical Pathophysiology in Parkinson's Disease. *J Neurosci* 37,
768 4830-4840.

769 Cole, S.R., and Voytek, B. (2017). Brain Oscillations and the Importance of Waveform Shape. *Trends*
770 *Cogn Sci* 21, 137-149.

771 Doelling, K.B., Assaneo, M.F., Bevilacqua, D., Pesaran, B., and Poeppel, D. (2019). An oscillator model
772 better predicts cortical entrainment to music. *Proc Natl Acad Sci U S A* 116, 10113-10121.

773 Donoghue, T., Haller, M., Peterson, E.J., Varma, P., Sebastian, P., Gao, R., Noto, T., Lara, A.H., Wallis,
774 J.D., Knight, R.T., *et al.* (2020). Parameterizing neural power spectra into periodic and aperiodic
775 components. *Nat Neurosci* 23, 1655-1665.

776 Douglas, R.J., and Martin, K.A. (2004). Neuronal circuits of the neocortex. *Annu Rev Neurosci* 27, 419-
777 451.

778 Eiermann, A., and Esser, K.H. (2000). Auditory responses from the frontal cortex in the short-tailed fruit
779 bat *Carollia perspicillata*. *Neuroreport* 11, 421-425.

780 Esser, K.H., and Eiermann, A. (1999). Tonotopic organization and parcellation of auditory cortex in the
781 FM-bat *Carollia perspicillata*. *Eur J Neurosci* 11, 3669-3682.

782 Folschweiller, S., and Sauer, J.F. (2023). Behavioral State-Dependent Modulation of Prefrontal Cortex
783 Activity by Respiration. *J Neurosci* 43, 4795-4807.

784 Garcia-Rosales, F., Beetz, M.J., Cabral-Calderin, Y., Kossl, M., and Hechavarria, J.C. (2018). Neuronal
785 coding of multiscale temporal features in communication sequences within the bat auditory cortex.
786 *Commun Biol* 1, 200.

787 Garcia-Rosales, F., Lopez-Jury, L., Gonzalez-Palomares, E., Cabral-Calderin, Y., and Hechavarria, J.C.
788 (2020). Fronto-Temporal Coupling Dynamics During Spontaneous Activity and Auditory Processing in the
789 Bat *Carollia perspicillata*. *Front Syst Neurosci* 14, 14.

790 Garcia-Rosales, F., Lopez-Jury, L., Gonzalez-Palomares, E., Cabral-Calderin, Y., Kossl, M., and
791 Hechavarria, J.C. (2022a). Phase-amplitude coupling profiles differ in frontal and auditory cortices of bats.
792 *Eur J Neurosci* 55, 3483-3501.

793 Garcia-Rosales, F., Lopez-Jury, L., Gonzalez-Palomares, E., Wetekam, J., Cabral-Calderin, Y., Kiai, A.,
794 Kossl, M., and Hechavarria, J.C. (2022b). Echolocation-related reversal of information flow in a cortical
795 vocalization network. *Nat Commun* 13, 3642.

796 Garcia-Rosales, F., Rohrig, D., Weineck, K., Rohm, M., Lin, Y.H., Cabral-Calderin, Y., Kossl, M., and
797 Hechavarria, J.C. (2019). Laminar specificity of oscillatory coherence in the auditory cortex. *Brain Struct*
798 *Funct* 224, 2907-2924.

799 Gourevitch, B., Martin, C., Postal, O., and Eggermont, J.J. (2020). Oscillations in the auditory system and
800 their possible role. *Neurosci Biobehav Rev* 113, 507-528.

801 Gross, J., Schnitzler, A., Timmermann, L., and Ploner, M. (2007). Gamma oscillations in human primary
802 somatosensory cortex reflect pain perception. *PLoS Biol* 5, e133.

803 Hechavarria, J.C., Beetz, M.J., Macias, S., and Kossl, M. (2016). Vocal sequences suppress spiking in
804 the bat auditory cortex while evoking concomitant steady-state local field potentials. *Sci Rep* 6, 39226.

805 Helfrich, R.F., and Knight, R.T. (2019). Cognitive neurophysiology of the prefrontal cortex. *Handb Clin*
806 *Neurol* 163, 35-59.

807 Henry, M.J., and Obleser, J. (2012). Frequency modulation entrains slow neural oscillations and
808 optimizes human listening behavior. *Proc Natl Acad Sci U S A* 109, 20095-20100.

809 Hilgetag, C.C., Beul, S.F., van Albada, S.J., and Goulas, A. (2019). An architectonic type principle
810 integrates macroscopic cortico-cortical connections with intrinsic cortical circuits of the primate brain.
811 *Netw Neurosci* 3, 905-923.

812 Hooks, B.M., Hires, S.A., Zhang, Y.X., Huber, D., Petreanu, L., Svoboda, K., and Shepherd, G.M. (2011).
813 Laminar analysis of excitatory local circuits in vibrissal motor and sensory cortical areas. *PLoS Biol* 9,
814 e1000572.

815 Insel, N., Patron, L.A., Hoang, L.T., Nematollahi, S., Schimanski, L.A., Lipa, P., and Barnes, C.A. (2012).
816 Reduced gamma frequency in the medial frontal cortex of aged rats during behavior and rest: implications
817 for age-related behavioral slowing. *J Neurosci* 32, 16331-16344.

818 Jackson, N., Cole, S.R., Voytek, B., and Swann, N.C. (2019). Characteristics of Waveform Shape in
819 Parkinson's Disease Detected with Scalp Electroencephalography. *eNeuro* 6.

820 Kanwal, J.S., Gordon, M., Peng, J.P., and Heinz-Esser, K. (2000). Auditory responses from the frontal
821 cortex in the mustached bat, *Pteronotus parnellii*. *Neuroreport* 11, 367-372.

- 822 Kienitz, R., Cox, M.A., Dougherty, K., Saunders, R.C., Schmiedt, J.T., Leopold, D.A., Maier, A., and
823 Schmid, M.C. (2021). Theta, but Not Gamma Oscillations in Area V4 Depend on Input from Primary
824 Visual Cortex. *Curr Biol* 31, 635-642 e633.
- 825 Kobler, J.B., Isbey, S.F., and Casseday, J.H. (1987). Auditory pathways to the frontal cortex of the
826 mustache bat, *Pteronotus parnellii*. *Science* 236, 824-826.
- 827 Koszeghy, A., Lasztozci, B., Forro, T., and Klausberger, T. (2018). Spike-Timing of Orbitofrontal Neurons
828 Is Synchronized With Breathing. *Front Cell Neurosci* 12, 105.
- 829 Kritzer, M.F., Cowey, A., and Somogyi, P. (1992). Patterns of inter- and intralaminar GABAergic
830 connections distinguish striate (V1) and extrastriate (V2, V4) visual cortices and their functionally
831 specialized subdivisions in the rhesus monkey. *J Neurosci* 12, 4545-4564.
- 832 Lakatos, P., Chen, C.M., O'Connell, M.N., Mills, A., and Schroeder, C.E. (2007). Neuronal oscillations and
833 multisensory interaction in primary auditory cortex. *Neuron* 53, 279-292.
- 834 Lakatos, P., Musacchia, G., O'Connell, M.N., Falchier, A.Y., Javitt, D.C., and Schroeder, C.E. (2013). The
835 spectrotemporal filter mechanism of auditory selective attention. *Neuron* 77, 750-761.
- 836 Lakatos, P., Shah, A.S., Knuth, K.H., Ulbert, I., Karmos, G., and Schroeder, C.E. (2005). An oscillatory
837 hierarchy controlling neuronal excitability and stimulus processing in the auditory cortex. *J Neurophysiol*
838 94, 1904-1911.
- 839 Linden, J.F., and Schreiner, C.E. (2003). Columnar transformations in auditory cortex? A comparison to
840 visual and somatosensory cortices. *Cereb Cortex* 13, 83-89.
- 841 Lopez-Jury, L., Mannel, A., Garcia-Rosales, F., and Hechavarría, J.C. (2020). Modified synaptic dynamics
842 predict neural activity patterns in an auditory field within the frontal cortex. *Eur J Neurosci* 51, 1011-1025.
- 843 Luo, H., and Poeppel, D. (2007). Phase patterns of neuronal responses reliably discriminate speech in
844 human auditory cortex. *Neuron* 54, 1001-1010.
- 845 Mara, M., and Julian, F.T. (2018). How heart rate variability affects emotion regulation brain networks.
846 *Current Opinion in Behavioral Sciences* 19, 98-104.
- 847 Medvedev, A.V., and Kanwal, J.S. (2004). Local field potentials and spiking activity in the primary auditory
848 cortex in response to social calls. *J Neurophysiol* 92, 52-65.
- 849 Mikutta, C., Wenke, M., Spiegelhalder, K., Hertenstein, E., Maier, J.G., Schneider, C.L., Feher, K.,
850 Koenig, J., Altorfer, A., Riemann, D., *et al.* (2022). Co-ordination of brain and heart oscillations during
851 non-rapid eye movement sleep. *J Sleep Res* 31, e13466.
- 852 Mochizuki, Y., Onaga, T., Shimazaki, H., Shimokawa, T., Tsubo, Y., Kimura, R., Saiki, A., Sakai, Y.,
853 Isomura, Y., Fujisawa, S., *et al.* (2016). Similarity in Neuronal Firing Regimes across Mammalian Species.
854 *J Neurosci* 36, 5736-5747.
- 855 Mountcastle, V.B. (1997). The columnar organization of the neocortex. *Brain* 120 (Pt 4), 701-722.
- 856 Neymotin, S.A., Tal, I., Barczak, A., O'Connell, M.N., McGinnis, T., Markowitz, N., Espinal, E., Griffith, E.,
857 Anwar, H., Dura-Bernal, S., *et al.* (2022). Detecting Spontaneous Neural Oscillation Events in Primate
858 Auditory Cortex. *eNeuro* 9.
- 859 Pandya, D.N., and Yeterian, E.H. (1996). Comparison of prefrontal architecture and connections. *Philos*
860 *Trans R Soc Lond B Biol Sci* 351, 1423-1432.
- 861 Passingham, R.E., Stephan, K.E., and Kotter, R. (2002). The anatomical basis of functional localization in
862 the cortex. *Nat Rev Neurosci* 3, 606-616.

863 Pittman-Polletta, B.R., Wang, Y., Stanley, D.A., Schroeder, C.E., Whittington, M.A., and Kopell, N.J.
864 (2021). Differential contributions of synaptic and intrinsic inhibitory currents to speech segmentation via
865 flexible phase-locking in neural oscillators. *PLoS Comput Biol* 17, e1008783.

866 Rajan, A., Siegel, S.N., Liu, Y., Bengson, J., Mangun, G.R., and Ding, M. (2019). Theta Oscillations Index
867 Frontal Decision-Making and Mediate Reciprocal Frontal-Parietal Interactions in Willed Attention. *Cereb*
868 *Cortex* 29, 2832-2843.

869 Ray, S. (2015). Challenges in the quantification and interpretation of spike-LFP relationships. *Curr Opin*
870 *Neurobiol* 31, 111-118.

871 Ruiz-Mejias, M., Ciria-Suarez, L., Mattia, M., and Sanchez-Vives, M.V. (2011). Slow and fast rhythms
872 generated in the cerebral cortex of the anesthetized mouse. *J Neurophysiol* 106, 2910-2921.

873 Schaworonkow, N., and Nikulin, V.V. (2019). Spatial neuronal synchronization and the waveform of
874 oscillations: Implications for EEG and MEG. *PLoS Comput Biol* 15, e1007055.

875 Schaworonkow, N., and Voytek, B. (2021). Longitudinal changes in aperiodic and periodic activity in
876 electrophysiological recordings in the first seven months of life. *Dev Cogn Neurosci* 47, 100895.

877 Shepherd, G.M. (2009). Intracortical cartography in an agranular area. *Front Neurosci* 3, 337-343.

878 Shinomoto, S., Kim, H., Shimokawa, T., Matsuno, N., Funahashi, S., Shima, K., Fujita, I., Tamura, H.,
879 Doi, T., Kawano, K., *et al.* (2009). Relating neuronal firing patterns to functional differentiation of cerebral
880 cortex. *PLoS Comput Biol* 5, e1000433.

881 Tan, L.L., Oswald, M.J., Heintz, C., Retana Romero, O.A., Kaushalya, S.K., Monyer, H., and Kuner, R.
882 (2019). Gamma oscillations in somatosensory cortex recruit prefrontal and descending serotonergic
883 pathways in aversion and nociception. *Nat Commun* 10, 983.

884 Tavares, L.C.S., and Tort, A.B.L. (2022). Hippocampal-prefrontal interactions during spatial decision-
885 making. *Hippocampus* 32, 38-54.

886 Teng, X., Tian, X., Rowland, J., and Poeppel, D. (2017). Concurrent temporal channels for auditory
887 processing: Oscillatory neural entrainment reveals segregation of function at different scales. *PLoS Biol*
888 15, e2000812.

889 Tort, A.B.L., Brankack, J., and Draguhn, A. (2018). Respiration-Entrained Brain Rhythms Are Global but
890 Often Overlooked. *Trends Neurosci* 41, 186-197.

891 Uran, C., Peter, A., Lazar, A., Barnes, W., Klön-Lipok, J., Shapcott, K.A., Roese, R., Fries, P., Singer, W.,
892 and Vinck, M. (2022). Predictive coding of natural images by V1 firing rates and rhythmic synchronization.
893 *Neuron* 110, 2886-2887.

894 Veniero, D., Gross, J., Morand, S., Duecker, F., Sack, A.T., and Thut, G. (2021). Top-down control of
895 visual cortex by the frontal eye fields through oscillatory realignment. *Nat Commun* 12, 1757.

896 Vinck, M., van Wingerden, M., Womelsdorf, T., Fries, P., and Pennartz, C.M. (2010). The pairwise phase
897 consistency: a bias-free measure of rhythmic neuronal synchronization. *Neuroimage* 51, 112-122.

898 Weineck, K., Garcia-Rosales, F., and Hechavarría, J.C. (2020). Neural oscillations in the fronto-striatal
899 network predict vocal output in bats. *PLoS Biol* 18, e3000658.

900 Zhang, S., Xu, M., Chang, W.C., Ma, C., Hoang Do, J.P., Jeong, D., Lei, T., Fan, J.L., and Dan, Y. (2016).
901 Organization of long-range inputs and outputs of frontal cortex for top-down control. *Nat Neurosci* 19,
902 1733-1742.

903

904

905 **Author Contributions**

906 F.G.R, N.S., and J.C.H. conceived and designed the research. F.G.R collected and analysed the data,
907 produced original figures, and wrote the first draft of the manuscript. F.G.R., N.S, and J.C.H. discussed
908 analyses and results, interpreted data, and reviewed figures and text.

909 **Figure legends**

910 **Figure 1. Spectral properties of local-field potentials in FAF and AC. (A) Left:** Schematic
911 representation of the probes used for recordings in FAF and AC. Depth and channel colours
912 correspond to those in panels **B** and **K**. **Middle:** Location of the FAF and AC in *C. perspicillata*'s
913 cortex. **Right:** Schematic representation of recording locations in AC, colour-coded by animal (blue:
914 Bat-01, N = 15; brown: Bat-02, N = 14). The precise location of one recording in Bat-02 could not be
915 recovered. **(B)** Cortical LFPs (5 s excerpts) recorded simultaneously from the FAF (left) and AC (right;
916 note that channel depths are colour-coded) of Bat-01. **(C)** Average power spectra in FAF across all
917 recordings (N = 15) in Bat-01 using full LFP traces (lengths of ~20 minutes), for all channels. The
918 spectrum of each channel is colour-coded according to the depth scheme of panels **A**, **B**. **(D)**
919 Parametrization of an exemplary power spectrum obtained from ~20 minutes LFP recordings in the
920 FAF (depth, 700 μm). LFP traces originate from the same recording shown in **B**. The 1/f fit is depicted
921 as a blue dashed line; power spectrum shown in solid black. **(E)** Normalized power spectra (to 1/f
922 activity) across all recordings in Bat-01, shown for channels located at 700 μm in FAF. Solid black line
923 indicates average (N = 15). **(F)** We tested whether the normalized power spectrum was significantly
924 larger than 0 (FDR-corrected t-test, $p_{\text{corr}} < 0.05$) across depths and frequencies. The t-statistics are
925 summarized here; values were set to 0 if the normalized power spectrum was not significantly (i.e.
926 $p_{\text{corr}} \geq 0.05$). **(G-J)** Similar to panels **C-F**, but data shown corresponds to channels located in the AC.
927 **(K-S)** Same as **B-J** but with data recorded from Bat-02.

928 **Figure 2. Burst cycle features and the coefficient of variation. (A)** Schematic representation of the
929 oscillatory burst detection algorithm. If at least 3 consecutive cycles fulfilled the detection parameters
930 (enclosed in the box), these cycles together were considered as an oscillatory burst (marked in
931 purple); otherwise, no burst was detected. No-burst cycles were not used in further analyses. **(B)**
932 Representative delta- and gamma-frequency bursting activity (bursts marked in purple) in the FAF
933 and AC, at a cortical depth of 700 μm . **(C)** Illustration of cycle waveform features: period, rise-decay
934 asymmetry, and peak-trough asymmetry. An artificial sinusoidal waveform was utilized for illustrative
935 purposes. **(D)** The median value for a given feature (e.g. period) across all cycles was used as the
936 value of that feature for a given LFP trace. The coefficient of variation across all feature values was
937 used as a measure of dispersion. Shown in the figure (in purple) is a schematic distribution of
938 feature values for a given LFP recording.

939 **Figure 3. Bursting dynamics and signal-to-noise ratio in frontal and auditory cortices. (A)**
940 Schematic illustrating the relationship of region and cortical depth with the channel number markers
941 of panels **B-G**. Notice that depths are colour-coded as in **Fig.1**. **(B) Top:** Distribution of signal-to-
942 noise ratio (SNR) shown for each channel (notice colour schemes in panel **A** for the region and
943 depth of each channel), across all recordings (N = 29 in FAF and AC). Values for Bat-01 are shown
944 with densities > 0; values for Bat-02 are shown with densities < 0 only for illustrative purposes.
945 **Bottom:** Effect sizes of channel-by-channel, pairwise statistical comparisons of SNR values (FDR-
946 corrected Wilcoxon signed-rank tests). Effect sizes for comparisons that did not yield significance
947 (i.e. $p_{\text{corr}} \geq 0.05$) were set to 0. A cell (*r*, *c*) in the effect size matrix indicates the effect size of the

948 comparison between burst proportion values in channel r and channel c (as per panel **A**). The
949 quadrant spanning rows [0–15] and columns [16–31] illustrates effect sizes of comparisons between
950 channels in FAF and AC. In this quadrant, red colours indicate higher proportion values in FAF. **(C)**
951 Same as in **B**, but data shown corresponds to burst proportions across recordings. **(D)** Same as in
952 **C**, but data shown correspond to burst durations (note the logarithmic scale of the x-axis).

953 **Figure 4. Burst co-occurrence in the FAF-AC circuit.** **(A)** Schematic representation of the analysis for
954 quantifying temporal co-occurrence of bursting events. Note that channels A and B could be drawn
955 from the same or different cortical regions. **(B) Left** (shaded green): indicates delta-band burst co-
956 occurrence across all channels, calculated relative to the onset of a burst at four representative
957 depths (50, 250, 450, 700 μm) in the FAF. Matrices in the top row show burst co-occurrence in FAF
958 channels; matrices in the bottom show co-occurrence of bursts in AC channels, aligned to burst
959 onsets in FAF (at $t = 0$). Burst co-occurrence values were z-normalized relative to a bootstrapped
960 baseline (blue colours: suppression of bursting activity; red colours: increased bursting activity). Only
961 z-normalized values considered significant ($|z| > 6$, see Methods) are shown. **Right** (shaded pink):
962 similar information, but in this case bursts originate in the AC at the same four representative depths
963 (50, 250, 450, 700 μm). Here, $t = 0$ is aligned to auditory cortical burst onsets. **(C)** Same as in **B**, but
964 depicting data related to the gamma frequency band. Note that burst co-occurrence matrices
965 corresponding to bursts originating within a specific area (i.e. FAF or AC) are shown with a different
966 colour scale than those corresponding to bursts originating outside a given area.

967 **Figure 5. Waveform shape differences between frontal and auditory cortical LFPs.** **(A)** Schematic
968 illustrating the relationship of region and cortical depth with the channel number markers of panels **B-**
969 **G**. Notice that depths are colour-coded as in **Fig. 1**. **(B) Top**: Distribution of oscillatory cycle periods
970 across all recordings ($N = 29$; for each recording, the median period across all cycles is considered),
971 for all channels (in FAF and AC; see panel **A** for region and depth according to colour), in the delta
972 band. Vertical lines indicate the median of each distribution. **Bottom**: Effect sizes of pairwise statistical
973 comparisons of population-level period values across all channels (FDR-corrected Wilcoxon signed-
974 rank tests). Effect sizes for comparisons that did not yield significance (i.e. $p_{\text{corr}} \geq 0.05$) were set to 0.
975 A cell (r, c) in the effect size matrix indicates the effect size of the comparison between values in
976 channel r and channel c (as per panel **A**). The quadrant spanning rows [0–15] and columns [16–31]
977 illustrates effect sizes of comparisons between channels in FAF and AC. In this quadrant, blue
978 colours indicate lower periods in FAF. **(C)** Same as in **B**, but corresponding to values of cycle feature
979 “rise-decay asymmetry”. **(D)** Same as in **C**, but related to values of cycle feature “peak-trough
980 asymmetry”. **(E-G)** Same as **B-D**, but shown for values obtained using gamma-band oscillatory
981 cycles.

982 **Figure 6. The variability of waveform shape features differs between frontal and auditory regions.**
983 **(A)** Schematic illustrating the relationship of region and cortical depth with the channel number
984 markers of panels **B-G**. Notice that depths are colour-coded as in **Fig.1**. **(b) Top**: Distribution of CV
985 values for oscillatory cycle periods across all recordings ($N = 29$), for all channels (in FAF and AC;
986 see panel **A** for region and depth according to colour), in the delta band. Vertical lines indicate the
987 median of each distribution. **Bottom**: Effect sizes of pairwise statistical comparisons of population CV
988 values across all channels (FDR-corrected Wilcoxon signed-rank tests). Effect sizes for comparisons
989 that did not yield significance (i.e. $p_{\text{corr}} \geq 0.05$) were set to 0. A cell (r, c) in the effect size matrix
990 indicates the effect size of the comparison between CV values in channel r and channel c (as per
991 panel **A**). The quadrant spanning rows [0–15] and columns [16–31] illustrates effect sizes of
992 comparisons between channels in FAF and AC. In this quadrant, blue colours indicate lower CV
993 values in FAF. **(C)** Same as in **B**, but corresponding to CV values of cycle feature “rise-decay
994 asymmetry”. **(D)** Same as in **C**, but related to CV values of cycle feature “peak-trough asymmetry”.

995 (E-G) Same as B-D, but shown for CV values obtained using gamma-band oscillatory cycles. (Effect
996 sizes can be interpreted as follows: $|d| < 0.5$ small, $0.5 \leq |d| \leq 0.8$ medium, $|d| > 0.8$ large).

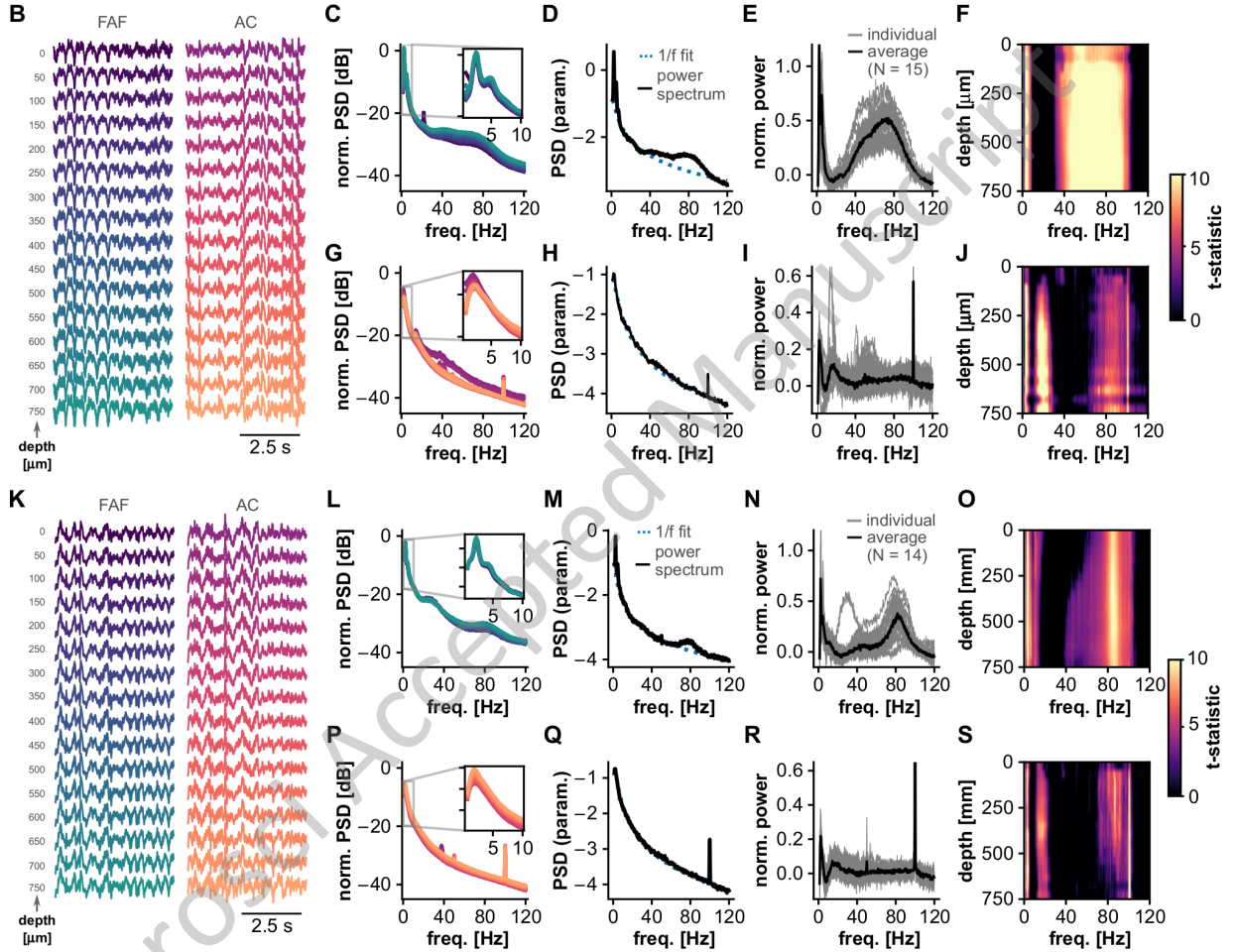
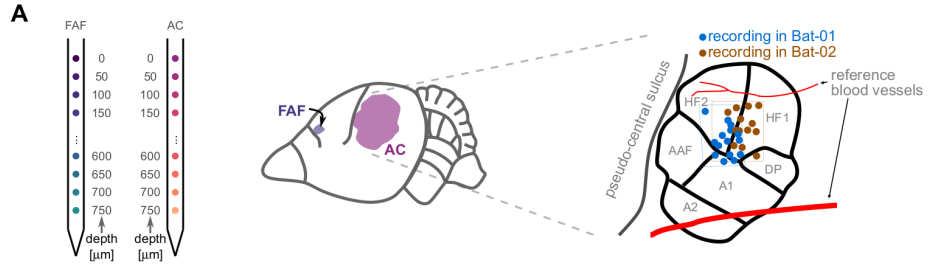
997 **Figure 7. Differences in waveform shape features and their variability are robust against burst**
998 **detection amplitude threshold.** The burst detection parameter “amplitude fraction threshold” was
999 varied independently in FAF and AC to determine whether SNR critically contributes to differences in
1000 oscillatory regularity between frontal and auditory areas. The difference across regions was measured
1001 as the median effect size obtained from comparing all pairs of channels in FAF and AC (e.g. median of
1002 the upper right quadrant in the comparison matrices in **Fig. 5**, labelled “inter-areal comparisons”). In
1003 the absence of significant differences (FDR-corrected Wilcoxon signed rank tests, $p_{\text{corr}} < 0.05$), effect
1004 size values were set to 0 ($p_{\text{corr}} \geq 0.05$). **(A)** Median effect sizes across all values of amplitude fraction
1005 threshold tested in FAF and AC, for delta frequencies, comparing the median of cycle periods (left),
1006 cycle rise-decay asymmetries (middle) and cycle peak-trough asymmetries (right). **(B)** Same as in **A**,
1007 but data corresponds to cycles from gamma-band oscillatory bursts. **(C, D)** Same as in **a, b**, but the
1008 CV was calculated across cycle periods. Red squares indicate the amplitude fraction threshold values
1009 used to detect bursts used in the main results.

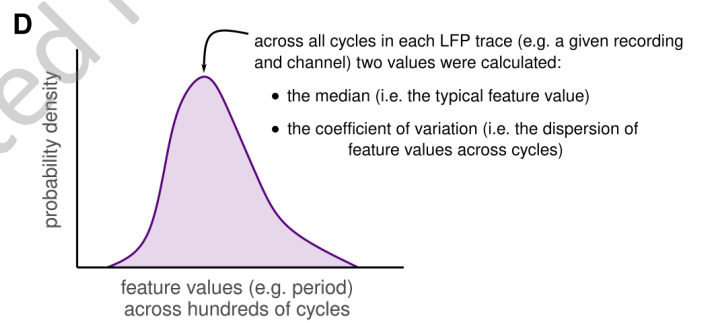
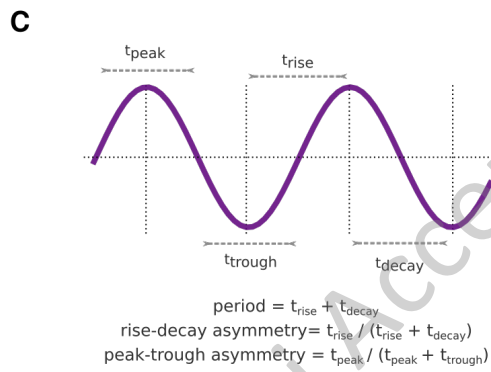
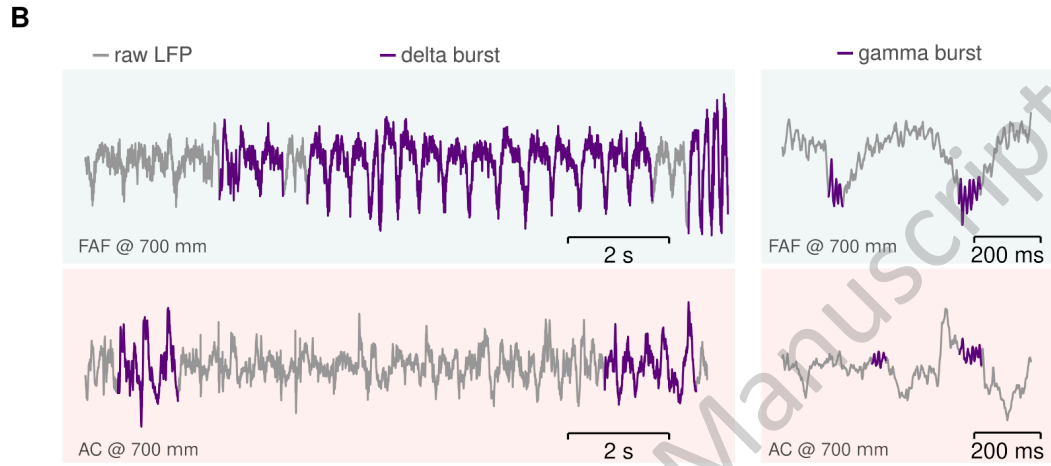
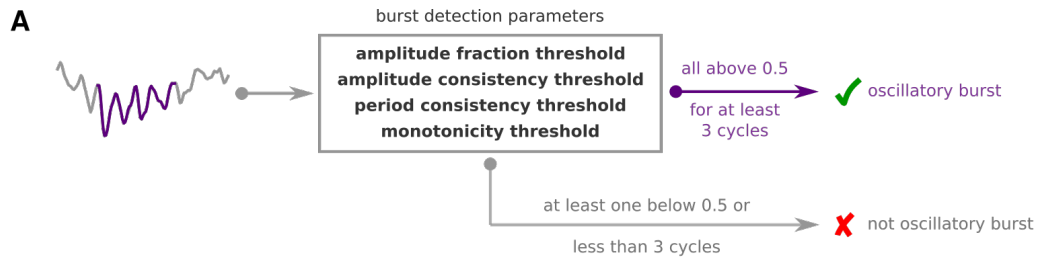
1010 **Figure 8. A linear model captures the differences in waveform shape between FAF and AC. (A)**
1011 Schematic illustrating how synthetic LFP signals were derived from the spiking activity of a population
1012 of simulated neurons. **(B)** Representative spiking activity of a population of $N=30$ simulated neurons.
1013 The synchronicity across neurons varies with the duty cycle of a pulse train modulating firing rate
1014 (lower duty cycle, more synchronous; see Methods). A synthetic LFP was calculated for each
1015 condition (overlaid traces; see panel **A**). **(C-E)** The period **(C)**, rise-decay asymmetry **(D)**, and peak-
1016 trough asymmetry **(E)** values across all cycles detected by the *bycycle* algorithm for each duty cycle
1017 tested. The black line in panels **D** and **E** represents no asymmetry (i.e. a value of 0.5). **(F-H)** CV
1018 values of features period **(F)**, rise-decay asymmetry **(G)**, and peak-trough asymmetry **(H)**. In panels
1019 **C-H**, values from each duty cycle simulation are colour coded according to panel **B**.

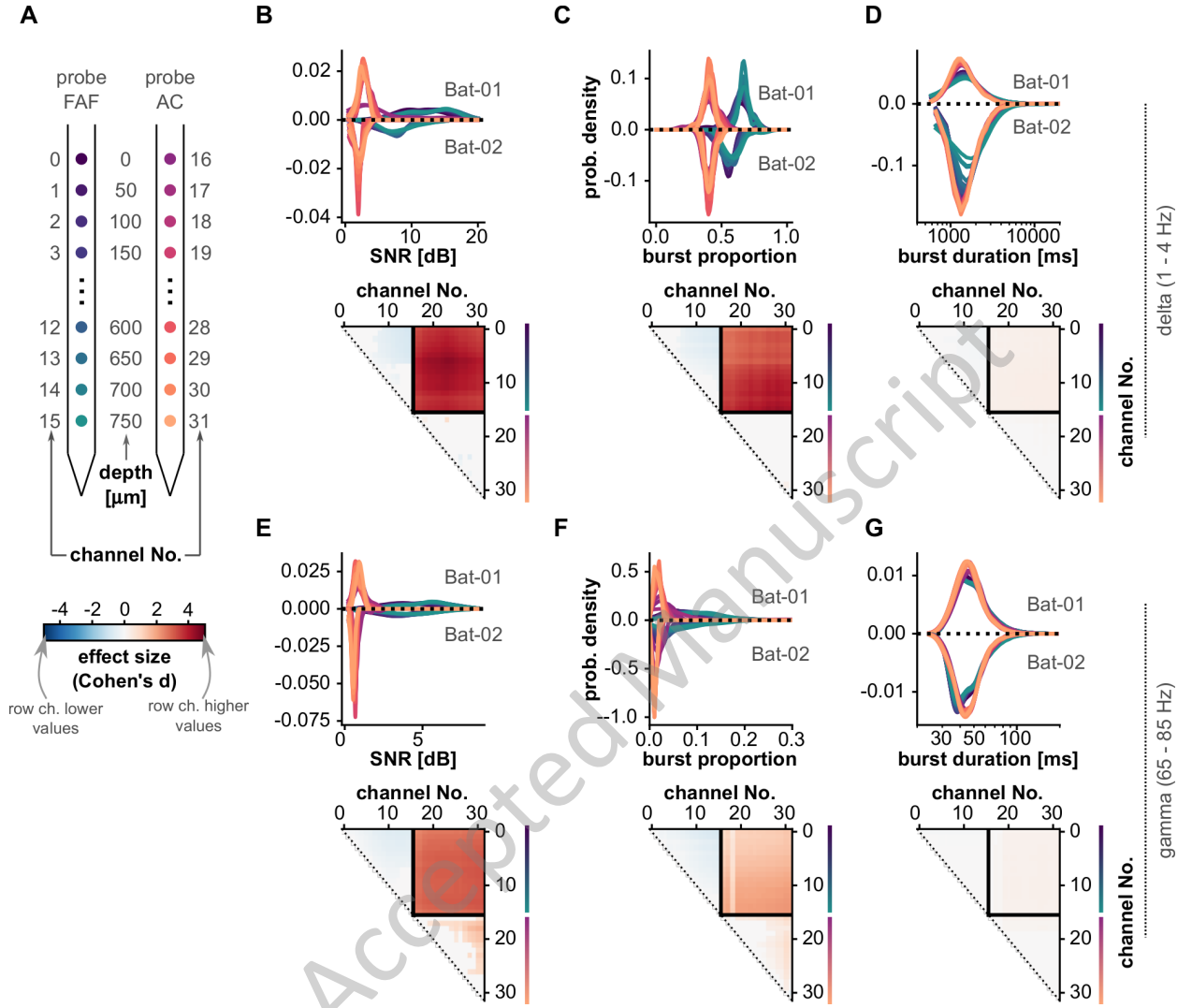
1020 **Figure 9. Spiking activity in FAF is more correlated and more strongly synchronized to delta-band**
1021 **oscillatory bursts. (A)** Representative LFP (top) and spiking (bottom) activity from FAF (purple) and
1022 AC (green) electrodes at depths of $700 \mu\text{m}$. **(B)** Spike-spike correlation coefficients for each recording
1023 in FAF and AC ($N = 29$; averaged across channels); spike-spike correlation in FAF was significantly
1024 larger than in AC (Wilcoxon signed-rank test, $p=2 \times 10^{-6}$, $d = 0.84$, large effect size). **(C)** Distribution of
1025 spike phases relative to delta LFPs in FAF (left, $N = 6760$ spikes) and AC (right, $N = 661$ spikes).
1026 Spikes were only those occurring during bursts of delta-band activity as detected by the *bycycle*
1027 algorithm. Troughs, peaks, rising and falling phases, for any given cycle, are indicated in the figure.
1028 **(D)** Average PPC values in FAF and AC were compared across all recordings ($N = 29$). There was
1029 significantly larger spike-phase consistency in FAF than in AC (Wilcoxon signed-rank test, $p=9.75 \times 10^{-4}$,
1030 $d = 0.96$, large effect size).

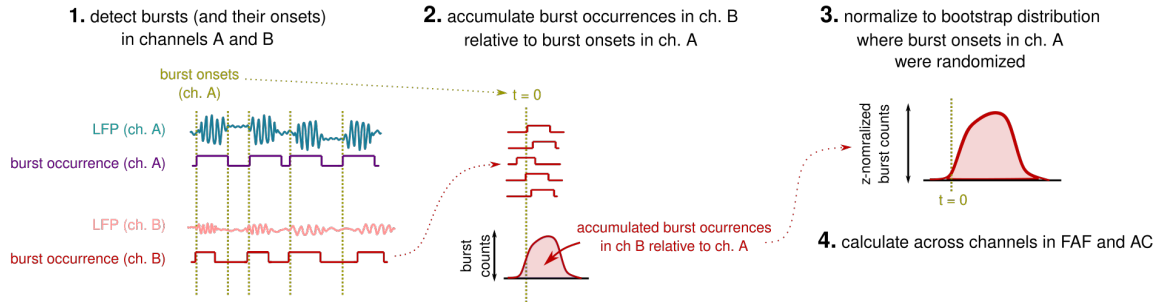
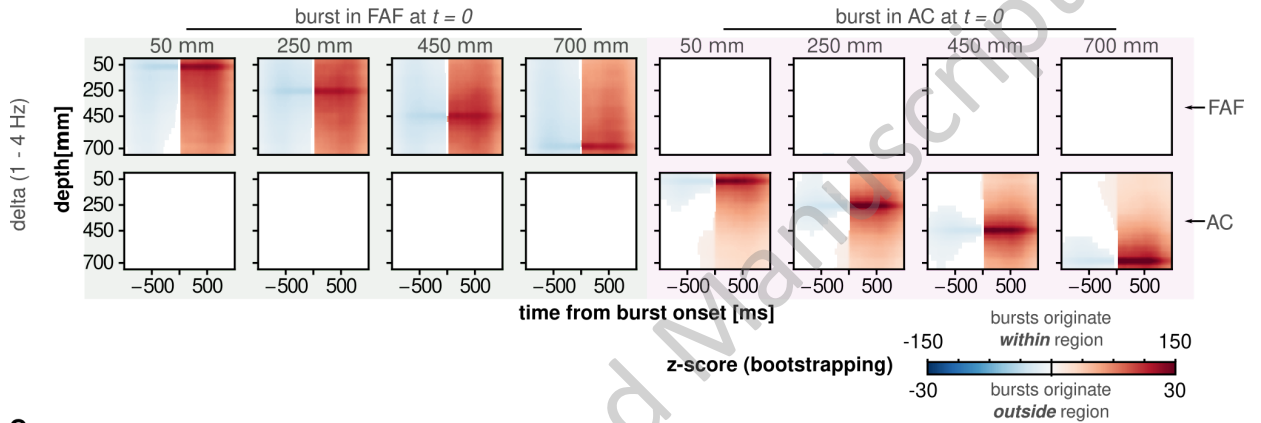
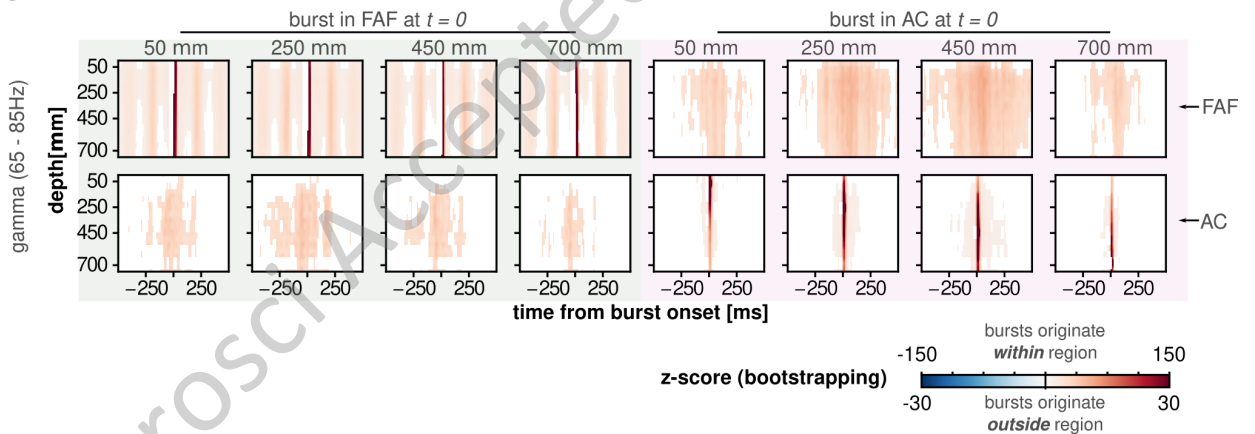
1031

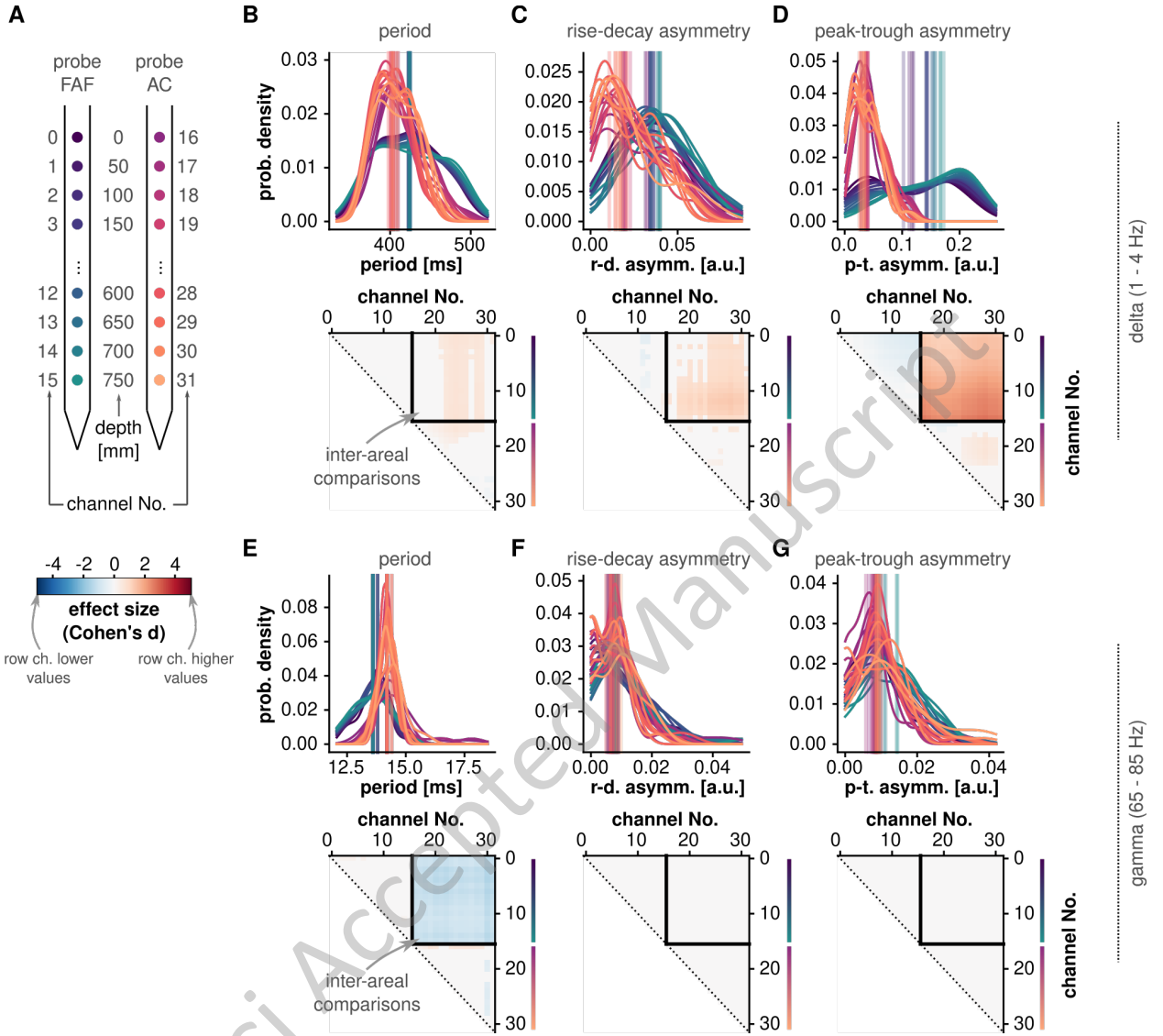
1032

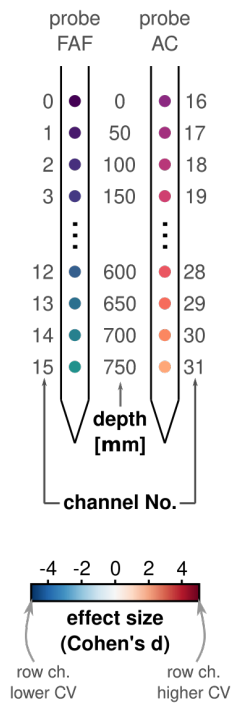
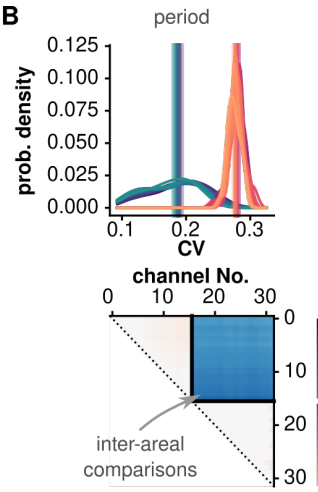
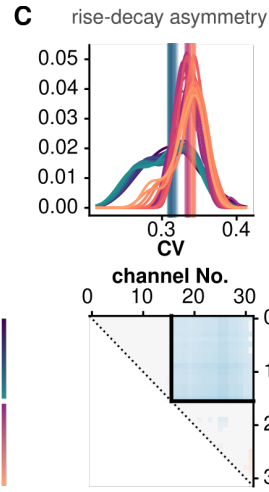
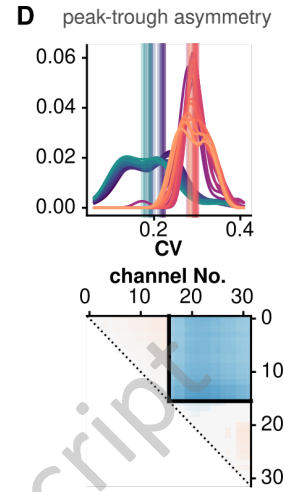
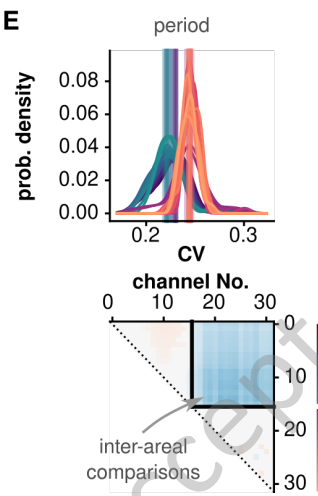
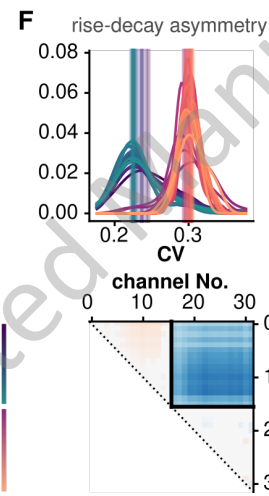
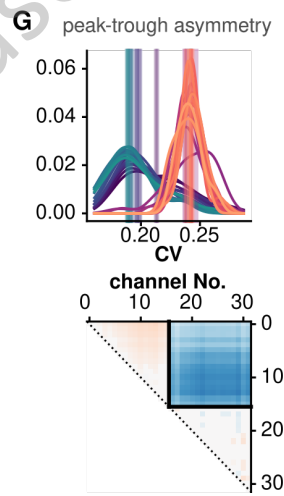






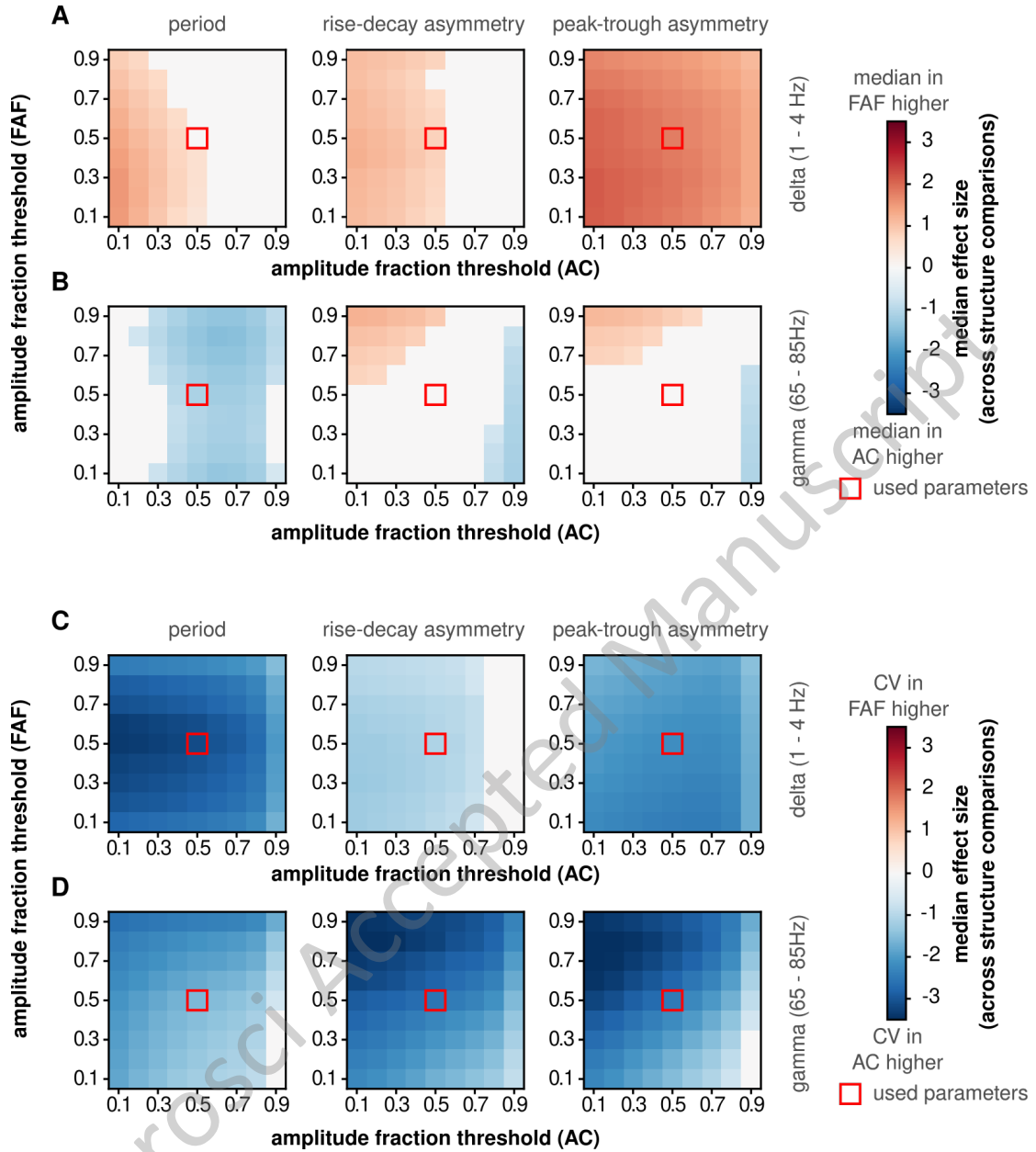
A**B****C**

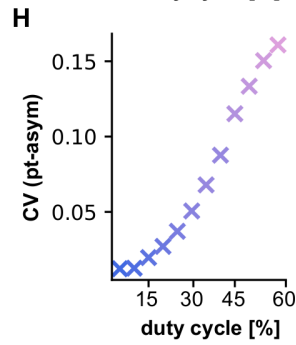
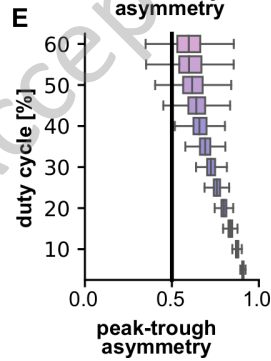
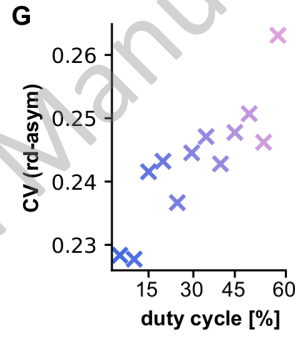
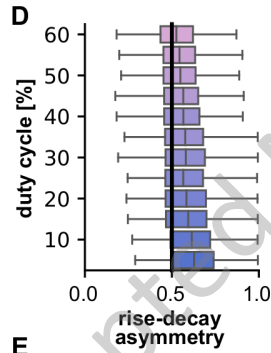
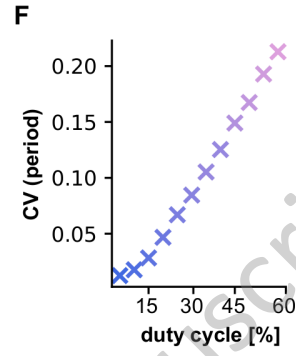
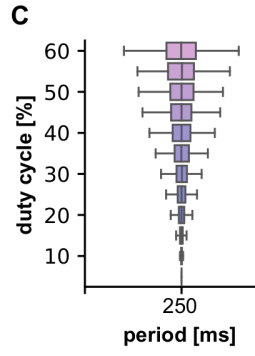
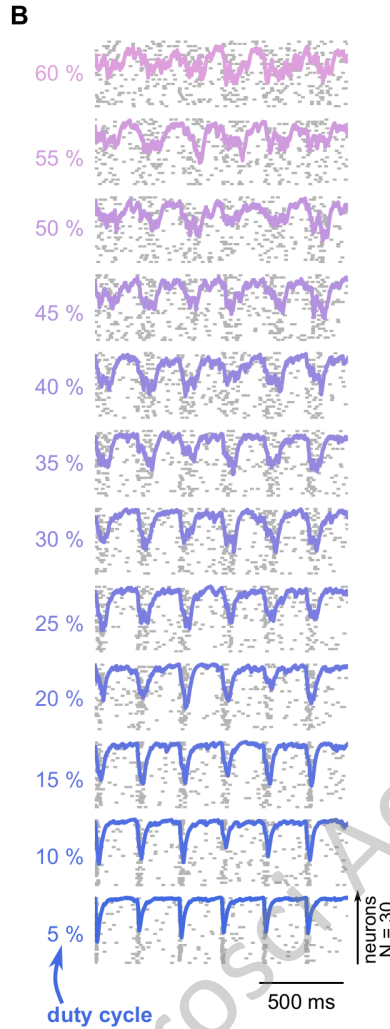
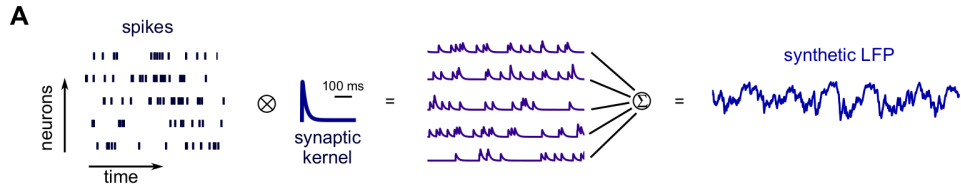


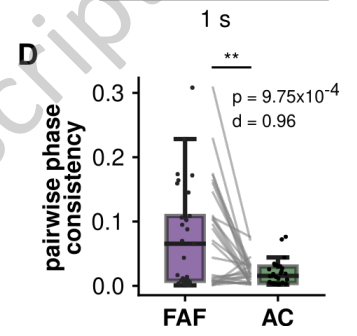
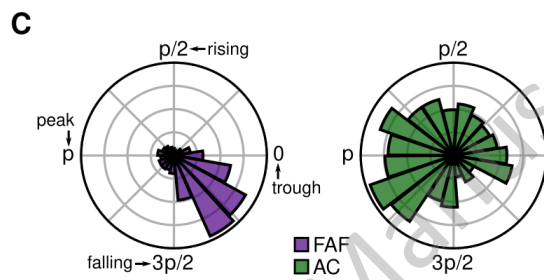
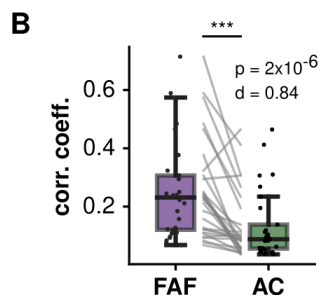
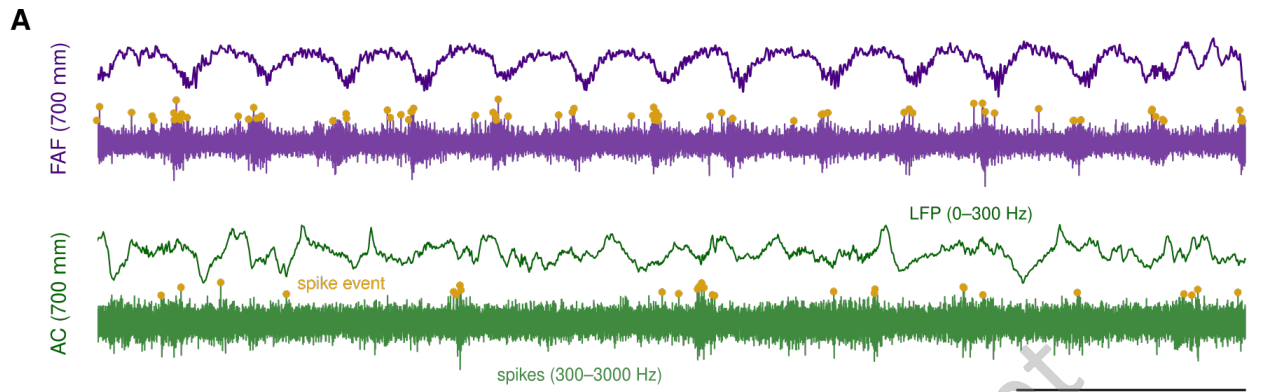
A**B****C****D****E****F****G**

delta (1 - 4 Hz)

gamma (65 - 85 Hz)







JNeurosci Accepted Manuscript